

S&G 3707

S&G3707 (Project 99/373)

**Modelling realistic ruptures on the
Wellington fault**

*Rafael Benites, Russell Robinson, Terry Webb,
Peter McGinty, IGNS*



Institute of
**GEOLOGICAL
& NUCLEAR
SCIENCES**
Limited



StG
3707

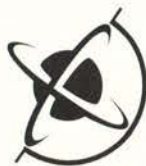
Modelling realistic ruptures on the Wellington fault

Confidential

Client Report
2002/85

by Rafael Benites, Russell Robinson, Terry Webb, Peter McGinty

November
2003



Institute of
**GEOLOGICAL
& NUCLEAR
SCIENCES**
Limited

Modelling realistic ruptures on the Wellington fault

by

**Rafael Benites
Russell Robinson
Terry Webb
Peter McGinty**

Prepared for

Earthquake Commission Research Foundation

CONFIDENTIAL

Institute of Geological & Nuclear Sciences client report 2003/85

Project Number: 410W9310

**The data presented in this Report are
available to GNS for other use from**

November 2003

November 2003

COMMERCIAL - IN - CONFIDENCE

This report has been prepared by the Institute of Geological & Nuclear Sciences Limited exclusively for and under contract to the Earthquake Commission Research Foundation. Unless otherwise agreed in writing, all liability of the Institute to any other party other than the Earthquake Commission Research Foundation in respect of the report is expressly excluded.



CONTENTS

EXECUTIVE SUMMARY	1
TECHNICAL ABSTRACT.....	3
1.0 INTRODUCTION	5
2.0 THE FAULT MODEL	8
3.0 MODELLING A SMOOTH WELLINGTON FAULT RUPTURE	9
4.0 MODELLING A COMPLEX RUPTURE OF THE WELLINGTON FAULT	10
4.1 Slip time histories derived from a synthetic seismicity model.....	10
4.1.1 Method.....	10
4.1.2 Scenario events and comparison with world-wide data.....	11
4.2 Modelling methodologies	12
4.2.1 Implementation of the finite fault approach at subfault level.....	12
4.2.1.1 Results	15
4.2.2 Implementation of the point source with directivity model.....	18
4.2.2.1 Results	20
5.0 SUMMARY AND CONCLUSIONS	22
6.0 ACKNOWLEDGEMENTS	24
7.0 REFERENCES	24
8.0 APPENDIX	44



EXECUTIVE SUMMARY

(Non-Technical Abstract)

The aim of this project was to realistically simulate a rupture of the Wellington fault. This is a difficult problem because, while we have a reasonable understanding of the low frequency behaviour (say 2–100 seconds period) of fault ruptures, we are not able to accurately model the high frequency behaviour (above ~1 Hz). Our inability to model high frequencies stems mainly from a lack of knowledge of the fine detail of earthquake ruptures and how seismic waves propagate through the earth. Typical approaches in the past have been to model these two processes separately, to carefully match the seismograms where they overlap in frequency, and then to combine them.

Our approach differs from the more conventional approach in that we have used as a starting point some computer-generated Wellington fault ruptures that have been produced by a complex model of interacting fault patches (1,500 patches distributed uniformly over the fault). We have shown that these synthetic rupture models are consistent with real observations of the faulting in large shallow earthquakes world-wide. Thus, for the first time, we have available a sufficiently complex model to generate high-frequency strong ground motion seismograms.

Our aim is to produce realistic seismograms that can be used by the science and engineering community to improve building design or to estimate likely earthquake damage. The trick in doing this is to correctly add up the contribution of each of the 1,500 subfaults with the correct timing and faulting behaviour. This was the most difficult part of this project.

Our initial approach was to treat each of the 1,500 subfaults as a small fault in its own right with its own series of small earthquake ruptures that represent that fault's behaviour during the whole rupture. We have successfully implemented this, but it is very time consuming to compute the results. We then spent a lot of effort on improving the efficiency of the calculations and transferring them to run on a cluster of 21 fast PC's. Even so, it still takes at least one week to do the full rupture simulation for a single site. This is too slow if we are to undertake detailed investigations of the spatial pattern of shaking or to gain insight into what contributes to the different parts of the strong shaking that we observe.

An alternative approach has been to treat each of the 1,500 subfaults as a simple point radiating seismic energy and then applying a correction to make it look like a small fault that is rupturing. This is much faster than our first approach — as currently implemented, we can complete a calculation for a single site in 5 hours.

In spite of the computer time limitations, we have been able to obtain some results using the first approach mentioned above. The results are very encouraging in that we have generated seismograms (representing earth motion in terms of displacement, velocity, and acceleration)



that have realistic peak values compared to data from large shallow world-wide earthquakes. The method does show some deficiencies in addition to being slow. Firstly, there is an enhancement of shaking at frequencies related to the size of the subfaults. Secondly, our assumed model of the earth has very hard rock right to the surface and the way in which seismic waves die out with distance has not been included. This results in accelerations that are too high. Some of these deficiencies are relatively easy to correct.

The results from our second approach are also encouraging in that they produce similar predicted levels of ground shaking far more quickly than in the previous approach. This approach also seems to largely overcome problems related to the size of subfaults. The second approach, as currently implemented, also has a slight deficiency in that the seismograms do not closely match those produced by the first method. This is because the way the two methods smooth the high frequency seismic waves is slightly different. If this smoothing effect is more carefully matched we expect the results to be in much closer agreement.

In summary, we have made a lot of progress towards generating realistic estimates of the shaking that would be produced by a complex Wellington fault rupture. The methods we have developed still have some shortcomings that need to be addressed. It must also be remembered that the approach we have adopted cannot account for localised amplification effects produced by either topography or deep, soft soil layers. These problems are more difficult to solve and need alternative approaches.



TECHNICAL ABSTRACT

We have defined a 3-segment fault model for the Wellington fault based on geological evidence and the fault geometry. The model has a 75 km length, a 20 km width, and dips at 80° to the northwest. Purely horizontal dextral faulting has been assumed. Scaling relations suggest a likely magnitude of M_w 7.4–7.6. We have modelled a smooth rupture across this fault and generated synthetic seismograms for two near-fault sites to test the effect of fault geometry. These tests show that a 3-segment model gives noticeably different low frequency seismograms for near-fault stations. We interpret this as being due to changes in station location with respect to the radiation pattern from various parts of the fault as the rupture propagates past, highlighting the need to use accurate fault geometry and site locations to in turn generate reliable seismograms.

We have used synthetic seismicity models, based on the interaction between many fault patches, or subfaults, to generate detailed slip distributions for ruptures over the model fault plane. We have shown that these slip distributions are consistent with relations derived from large global earthquakes. We then treated each subfault in the synthetic seismicity model as a small finite fault, computed the radiation from that fault, and then summed over all subfaults to produce synthetic seismograms. We have found that this approach has two shortcomings. First, the calculations are very computer intensive. After a significant amount of effort improving efficiency, it still requires at least a week of computation to calculate the seismograms for a single site on a cluster of 21 fast PC's. More rapid turn-around is required for detailed studies of the predicted ground shaking and what factors affect it. The second shortcoming was that displacement spectra are enhanced over the 2–3.5 Hz range and then show a sudden decrease at frequencies related to the subfault size. Artefacts of this kind are not unexpected, but given that they are nearly two orders of magnitude in size they are quite undesirable if the synthetic seismograms are to be of practical use. We believe that the artefact is related to the frequencies produced by the starting and stopping of the ruptures across each individual subfault.

As a more practical alternative to the finite fault approach, we then treated each subfault as a point source, but included directivity through adding correction factors for the *P* and *S* waves. This reduced computation times on the PC cluster to about five hours, and also greatly reduced the artefact related to subfault size. This method, however, also seems to have some shortcomings. Waveforms and spectra differ significantly from the finite fault results. This is most likely to be due to the use of the same rise time as for the finite fault approach and can be remedied by adjusting the rise time so that the frequency content of the two approaches is matched.

Both methods of rupture summation produce displacement and velocity seismograms with peak amplitudes near to those expected, based on observations from global earthquakes. The only exceptions to this are the high accelerations due to very close asperities (regions of high slip). These warrant further investigation for a variety of rupture scenarios. Peak



accelerations tend to be a little high, but this is most likely to be due to using a model with high velocities (akin to very hard rock) near to the surface and the lack of any attenuation terms. A high priority for further work would be to improve the velocity model and to include the effects of attenuation. The models correctly reproduce clear fault-normal directivity pulses at low frequencies. In future work we hope to examine these in detail to look at their behaviour for a range of earthquake magnitudes and to see when the breakdown in directivity is occurring as a function of frequency.

We see the progress we have made in implementing two methods for summing subfault ruptures produced from a synthetic seismicity catalogue as a big step forward over other techniques that have had to rely on the synthesis of separate deterministic and stochastic approaches for low and high frequencies, respectively. We are very encouraged that both of our summation methods give reasonable values for near-fault motions in terms of peak displacement, velocity, and acceleration and, when more fully developed, will lead to more insight into the generation of strong ground motions. Both of our approaches, however, have some shortcomings that need further work to overcome. The most significant of these, and perhaps the most easily overcome, are the use of lower velocity surface layers (softer rock), the inclusion of attenuation terms, and suitable matching of frequency content across the two approaches by adjusting rise time duration.



1.0 INTRODUCTION

A potential rupture of the southern segment of the Wellington fault dominates the seismic risk for New Zealand. This comes about because of the fault length, and hence expected earthquake size, the fault's close proximity to several major cities, its shallow depth, and moderately high potential to rupture within the next few hundred years (~10% in 50 years; Rhoades *et al.*, 1994).

One of the largest unknowns in hazard models is the amplitude of ground shaking from a rupture of this type, in particular the amplitude of high frequency (few Hz) damaging shaking that will occur at different sites. This knowledge is important for predicting overall losses, and also for better design of infrastructure and for predicting how existing structures will perform. Typically the level of strong shaking near to faults is estimated from actual recordings from large earthquakes elsewhere in the world. But given that large surface-rupturing earthquakes are relatively rare and, on a global scale instrumentation is sparse, the number of useful strong motion records is quite limited. This situation will improve slowly as more strong motion instrumentation is installed and sufficient time elapses to record large events.

In the interim there is a need to improve estimates of near-fault strong-motions and it is in this area of research that both empirical and theoretical approaches can contribute. The empirical Green's function approach uses small earthquakes as empirical Green's functions (EGF's) to represent path and receiver effects as seismic waves propagate from the earthquake rupture to the receiver at the Earth's surface (Hartzell, 1978; Frankel, 1995). Large ruptures are simulated by appropriately scaling and summing the small events to account for the long period energy and coherence, respectively, of the large rupture. This method has the advantage that all path and near-receiver effects, such as topography and basins, are accounted for. It has the disadvantages that suitable EGF events may be rare, scaling and summing the small EGF events correctly can be difficult, and radiation pattern effects are difficult to account for correctly.

The EGF approach has been used recently by Pancha *et al.* (2002) to simulate a rupture on the Wellington fault. Both strong motion recordings of small events, and data collected by Victoria University and the Institute of Geological and Nuclear Sciences in microzoning projects, were used in their analysis. Pancha *et al.* (2002) had difficulty in determining accurate corner frequencies for the small EGF events, because they were smaller than ideal. Since the corner frequency is important for how one scales up the EGF events to large events, this could affect their result. They finally had to derive corner frequencies from recently derived scaling relations for New Zealand earthquakes (Webb *et al.*, 1998).

Finite difference codes have the advantage of providing a complete solution to the ground motion modelling problem, with accuracy limited only by available grid size, and hence the size of available computers and the size of the problem. For example, Wald *et al.* (1996a) have demonstrated that modelling the Landers earthquake as a heterogeneous rupture and propagating the resulting seismic radiation through realistic structures into the Los Angeles basin is a tractable problem. Unfortunately, size limitations limit this approach to periods



longer than 2s, which for the New Zealand situation are too low in frequency to be of much engineering significance. This problem will eventually be solved through use of variable finite difference grid sizes (e.g. Aoi *et al.*, 1998), after which the limitation will be our knowledge of the actual basin boundaries and geological structure, and the details of the source time history. The latter limitation is unlikely to ever be overcome, limiting the applicability of the technique, when applied on its own, to modelling the longer period motions that affect large structures.

A 3-D finite difference approach has been applied to modelling a M6.7 earthquake due to a rupture on part of the Wellington fault by Benites *et al.* (2000). This study modelled the wave propagation through the Wellington metropolitan area, considered to extend over an area of about 32 by 10 km, and containing the fault. Due to the lack of information regarding slip histories from other events on the fault, the slip history in this study was taken as that of the Landers earthquake (Wald *et al.*, 1996). The Wellington fault simulation was for up to 1.5 Hz and, although attenuation was incorporated in the numerical scheme (Day, 1998) the results show peak values for particle velocities that are too high (about 2.4 m/s). If attenuation was incorporated in a non-linear manner for propagation of seismic waves in the upper layer of the geological structure, we would expect the particle velocities to be reduced to more reasonable values.

Strong motion records of large earthquakes are now routinely inverted to determine the slip distributions on the fault plane when data coverage is sufficient (e.g. Wald, 1996). Such inversions usually use data in the 0.05–0.5 Hz bandwidth for which details in the waveforms due to source or structural complexities are not too severe to model, and split the mainshock fault into a rectangular grid of subfaults. These complexities may be introduced with smaller subfault size (i.e. a denser grid of subfaults) and variable rise time and slip for each of the subfaults. One can equivalently produce synthetic strong motion records by forward modelling a fault rupture and propagating the radiated seismic waves through a horizontally layered crustal velocity model to receivers on the Earth's surface. In the New Zealand context this approach was used by Abercrombie and Benites (1998) to model the strong motion seismograms recorded from the 1993 Tikokino earthquake. This approach implies linearity of the effects of the complexity of the fault across the frequency range, which may disregard the fact that low frequencies also arise from interactions among the subfaults. Another approach, which also implies linearity, is that by Dan and Sato (1999) to simulate broadband strong ground motion. The lower frequencies are modelled from variable slip rupture models for large earthquakes, obtained by the source inversion of long period (greater than 4 seconds) seismic waves. The higher frequencies (less than 4 second period) are incorporated by assuming the ω^{-2} model with two corner frequencies related to the temporal integration of the slip-velocity time function and the spatial integration of the slip-velocity time function on the subfault.

One approach is to utilise a hybrid technique whereby the low frequencies are modelled theoretically and the high frequencies are added through the inclusion of EGF events (Hartzell, 1978), which has been improved by further research. The crucial issue in the use of small earthquakes as empirical Green's functions is determining the difference between the



source time functions of the small and large event (i.e. scaling the source time function of the small earthquake up to the large earthquake — the so-called “scale factor”). Hartzell (1978) determined such difference by trial and error to fit the theoretical and observed seismic waveforms.

Kanamori (1979) associated the scaling factor with the ratio between the seismic moment of the small earthquake and the seismic moment of the subevents of the large earthquake to simulate long period strong ground motion. He proposed three ways to sum the empirical Green’s functions: simultaneous addition, uniform time delay, and random time delay.

Irikura (1983) used the uniform delay addition of Kanamori (1979) and assumed a similarity relationship of fault length, width and dislocation, and modelled correctly the 1980 M6.7 Izu-Hanto-Toho-Oki, Japan, earthquake for periods longer than one second. The method of Irikura (1983) has been further improved to incorporate higher frequencies (from 0.05 to 10 Hz) by Irikura (1986), Joyner and Boore (1988), Dan *et al.* (1990), Frankel (1995) and Kamae *et al.* (1998) by assuming the ω^{-2} source spectrum model.

The ideal goal of the semi-empirical methods is to infer the short-period source time functions of the subevents from the long-period source inversions, because a detailed inversion valid for both ranges is rare, and has been performed only for a few large earthquakes. Somerville *et al.* (1991) used Kanamori (1979) random delay addition and the ω^{-2} source spectrum model to infer the short-period source time functions. The rise time is assumed to be the same on all subfaults and the slip velocities are assumed to be proportional to the final slips.

Another approach for adding more complexity to a rupture time history is to use synthetic seismicity models to generate slip distributions (Robinson and Benites, 2001). Such models contain a time history of slip for each fault (and its subfaults), generated from the interaction between all subfaults and other faults. In this report we use this approach to generate synthetic seismograms for a Wellington fault earthquake.

We begin by developing a fault model applicable to the Wellington fault — source characterisation being a key factor in being able to accurately predict ground motions. The fault characterisation involves determining the length, width, and geometry of the fault.

We then model a smooth rupture of the Wellington fault. In our original proposal it had been our intent to use the smooth model as a basis for comparison with more detailed models and with empirical approaches. A smooth rupture, however, can not generate the high frequencies seen in empirical summations, so no effective comparisons can be made. The technique is useful, though, for looking at the effect of the fault geometry on the predicted ground motions at near-fault sites.

We then develop two detailed Wellington fault rupture scenarios using the synthetic seismicity approach (Robinson & Benites, 2001). The slip distributions from these scenarios are tested against known slip distribution characteristics to make sure that they agree with observations from other earthquakes. We then generate complex seismograms for the scenario events by summing over all sub-faults in the scenario models using two approaches.



In the first, each subfault is treated as a finite fault in its own right, hence explicitly including directivity. The problem with this method is that it is very computer intensive, so running many scenarios would be too time consuming. In the second approach, each subfault is treated as a point source, but directivity is included by applying corrections to the *P* and *S* waves. For both approaches the radiation is then propagated through a horizontally layered structure. Horizontally layered velocity models should be a good representation of some parts of the Wellington region, but they will not account for the effects of steep topography or sedimentary basins. Modelling the effect of topography and basins in three dimensions is far from trivial, and is a problem we hope to address in future research.

Finally, we analyse our synthetic data to see whether its characteristics follow that of world-wide data from other large earthquakes.

2.0 THE FAULT MODEL

Our model for a Wellington fault earthquake is based on treating the Wellington-Hutt Valley segment of the Wellington fault as a contiguous segment. The northern end is taken to be at a pull-apart basin (the Kaitoke basin; Fig. 1) where a 2 km right step occurs and there is a significant change in strike (Berryman, 1990). The southern end is the limit to where the fault can be structurally traced offshore into Cook Strait (Carter *et al.*, 1988). This gives a total segment length of 75 km (Berryman, 1990). The timing of paleo earthquakes also supports the idea that this is a single contiguous segment in terms of earthquake ruptures in that dates obtained from each (on land) end of the fault are similar (Van Dissen *et al.*, 1992).

We use a fault width of 20 km for the model, similar to the 22 km used by Pancha *et al.* (2002). Microseismicity data (Robinson, 1986) indicate that the full crustal width is seismogenic in this location so the fault width is limited by the depth of the plate interface. The depth to the top of the subducting Pacific plate in the Wellington region, as determined by cross-sections of microseismicity and the occurrence of small reverse-faulting earthquakes, is 22–25 km (Robinson, 1986; Reyners *et al.*, 1997). We arbitrarily limit the width to 20 km, ending the fault a little above the plate interface. If the Wellington fault had aseismic slip at depth, this would further reduce its effective seismogenic width. Recent GPS modelling, however, produced no evidence for any significant deep slip on the Wellington fault (Darby & Beavan, 2002).

The Wellington fault generally has the highest topography on its north-western side, so given the compressional environment, it is expected to dip slightly to the north-west. A dip of 90° has been assumed for the rupture model to simplify the calculations. A steep dip is expected given that the fault is relatively straight and is predominantly strike slip. Geological evidence suggests that the vertical motion is less than 10% of the horizontal (Berryman, 1990), so a rake of 180° has been assumed.

Pancha *et al.* (2002) approximated the Wellington-Hutt Valley segment with a single straight segment (Fig. 1). In this study, we compare the single segment model with a more complex



3-segment model that approximates the actual fault trace much more accurately. The three segments are chosen and oriented to approximate the actual fault trace (derived from Van Dissen *et al.*, 1992 and Carter *et al.*, 1988) to within ± 6 km. To aid in the comparison of synthetic seismograms, the Pancha *et al.* (2002) model is also segmented in a similar way to our 3-segment model, but with all segments aligned. Figure 1 shows the segmentation models and Table 1 lists the associated parameters.

Our velocity model assumes horizontal layers and is based on the Robinson (1986) velocity model for the Wellington region (Table 2). From the Robinson (1986) model we retain the surface layer (thickness 0.4 km) and amalgamate other crustal layers so that our fault can be contained within a single layer. The amalgamated layer has P and S wave velocities in proportion to the layers in the Robinson (1986) model that are combined to make up the equivalent new layer (Table 3).

3.0 MODELLING A SMOOTH WELLINGTON FAULT RUPTURE

To model a smooth rupture on the Wellington fault we use the discrete wave number representation of a finite fault developed by Bouchon (1979). This has been adapted (Abercrombie & Benites, 1998) for arbitrary fault orientations, arbitrary rupture parameters, layered media using generalised reflection and transmission coefficients (Kennett 1983; Chin & Aki, 1991) and a prescribed rupture velocity. The total wavefield radiated by the fault is computed by adding up the wave contributions of elementary double-couple point sources regularly distributed over the entire fault plane using dilatational and rotational potentials. We assume harmonic time-dependency, so the wavefield representation is in the frequency domain. Time domain seismograms are obtained by using a ramp-like slip time function (Ben-Menahem and Singh, 1981). Calculations are done for 512 frequencies ranging from 0 to 4.27 Hz, corresponding to a total seismogram duration of 60 s.

We model a smooth rupture that initiates in the south and propagates to the north with uniform rupture velocity and slip. We use a rupture velocity of 0.8 of the S-wave velocity in the layer that contains the fault plane (e.g. Wald *et al.*, 1996b).

In our original proposal the intent of modelling a smooth rupture was to be able to make comparisons with the EGF results of Pancha *et al.* (2002). However, a smooth rupture of a long fault is not able to generate high frequencies. Typically the time constants involved are the rise time (or ramp slip time function) and the rupture duration. For our model these time constants are 0.5 s and 27 s respectively. The effective bandwidth of the Pancha *et al.* (2002) EGF data is typically 3–20 Hz, so their data provide no information on the longer periods that we are modelling. We thus cannot make any useful comparisons.



Smooth rupture models do allow us to investigate the effect of fault geometry on seismograms synthesised for near-fault stations. We investigate the significance of having more complex rupture geometries by segmenting the fault to more closely follow its actual geometry, as described above (Section 2.0). We use three models: a single straight segment; a straight segment partitioned into three subsections; and three subsections with varying strikes (Fig. 1 and Table 1).

In Figure 2 we show displacement seismograms calculated for each segmentation model, with seismograms synthesised for two sites near to the fault at each end of Wellington harbour. These sites have been chosen because they have strong motion recorders and are quite close to the fault (especially WEL), so may eventually provide data from a real Wellington fault rupture. For each subsection of fault, seismograms are calculated for a smooth rupture and then each subsection is offset in time according to the distance from the rupture initiation and the rupture velocity. The three subsections are then summed together to form a composite seismogram.

For the single segment and aligned segments, we find that the resulting waveforms are identical (Fig. 2), showing that our method of breaking up the fault into sub-sections and then summing them together is valid. The seismograms for the fault model that deviates from a linear fault through varying the strike of the subsections are more complex in detail than those for the linear rupture model (Fig. 2). We attribute this to the closeness of the sites to the fault — in the variable strike model, sites can be on either side of the projection of the rupturing fault as the rupture develops, depending on which segment is rupturing. This can effectively result in some cancellation of the fault-parallel motion, hence the reduced amplitudes seen on that component. The distance from the station to the closest piece of fault may also be a factor (noting that amplitudes at GNS are lower than at WEL), but one that will affect high frequencies more than the frequencies being generated by this model.

Some directivity effects are also noticeable in Figure 2 in that the fault-normal components of displacement are larger than the fault-parallel ones. The effect is not large, however, because the stations are located near to the centre of the rupture rather than being at one end.

4.0 MODELLING A COMPLEX RUPTURE OF THE WELLINGTON FAULT

4.1 Slip time histories derived from a synthetic seismicity model

4.1.1 Method

The time history of slip for a large event on the Wellington fault has been derived using the synthetic seismicity techniques of Robinson & Benites (1995, 1996 & 2001). The fault is modelled as a 75 by 20 km plane, with a 90° dip and extending to the surface. Building the synthetic seismicity model using a 3-segment fault would add a great deal of complexity to the calculations. The slip time history from the planar fault can easily be projected on to the three segments so that the geometry is accurate for the rupture calculations, which directly affect the radiation pattern. Similar arguments apply to the use of a 90°, rather than 80°, dip.



The geometry affects the synthetic seismicity calculations to a lesser degree because it mainly affects distances between cells on the fault plane.

The planar fault is subdivided into 1 x 1 km cells, each of which obeys a modified Coulomb friction law. When a cell fails it induces changes in stress (normal and shear) on all other cells after an appropriate time (the distance divided by the shear wave velocity). The stress on the fault evolves through time due to these elastic interactions between the individual cells and due to a constant background increment in horizontal shear stress. Mechanical properties of the fault (Table 4) are chosen, largely by trial-and-error, so that single cell failures often cascade into large “characteristic” events, as observed in reality for the Wellington fault. The mechanical properties are also adjusted so that the average slip in a model event is roughly the same as that derived from paleoseismology studies, and so that the distribution of asperities (in this work taken to be regions of higher than average co-seismic slip) matches that of world-wide events (Somerville *et al.*, 1999). The friction law is modified from a simple static/dynamic type to enforce healing after 3 seconds (maximum), as observed for similarly large world-wide events (Heaton, 1990; Somerville *et al.*, 1999). Time resolution during ruptures is 0.01 second.

4.1.2 Scenario events and comparison with world-wide data

The synthetic seismicity program generates multiple events, following on one after another. Some of these events are large “characteristic” events, while many are not. For our purposes we require large “characteristic” events and so have chosen two of these from the synthetic catalogue rather than any of the many smaller events. The first large event chosen was selected because the rupture initiated near one end of the fault and is thus representative of a unilateral rupture. Studies of global earthquakes have shown that unilateral ruptures predominate over bilateral ones (McGuire *et al.*, 2002). The second event is representative of a bilateral rupture.

Various properties of Events 1 and 2 are given in Tables 5 and 6, respectively, along with values predicted by the regressions of Somerville *et al.* (1999) for events of the same moment. Somerville *et al.* (1999) have used earthquake slip distributions, derived from slip inversions for large earthquakes, to characterise slip distribution parameters such as area, slip, area of asperities, slip in asperities, and variability of slip, as a function of seismic moment. In general there is good agreement between the parameters. The largest discrepancy is for overall rupture area, which is small for our synthetic events compared to the world-wide regressions. When the synthetic event data are plotted with the Somerville *et al.* (1999) data, however, the values are not unreasonable given the scatter in the world-wide data. A smaller area requires larger slip to give an equivalent moment and hence implies larger stress drop. A higher than average stress drop is not unreasonable for the Wellington fault given that it has a relatively low slip rate (~6 mm/yr; Berryman, 1990) and small total offset (~10–12 km; Stirling *et al.*, 1996).

A further comparison with world-wide data sets can be made with parameters derived from moment-area scaling relations. Hanks and Bakun (2002) have recently derived a M_0 -area relation for fast-slipping plate boundary faults. This relation specifically addresses the issue



of width-limited ruptures, so is applicable to the Wellington fault. For the Wellington fault the relation gives M_w 7.4 with an average slip of 3.0 m. This agrees reasonably well with our synthetic models and is slightly less than paleoseismology estimates (3.2–4.7 m; Van Dissen *et al.*, 1992).

New Zealand earthquake source duration data have recently been used to determine a moment-length relationship for low slip rate (<5 mm/yr) regions (Webb, pers. comm., 2002). This relationship also specifically addresses width-limited ruptures. For the Wellington fault this relation gives M_w 7.5 with an average slip of 5.9 m. This is much greater than predicted by the synthetic seismicity model and a little greater than paleoseismology estimates, although slip at depth is likely to be larger than at the surface. Furthermore, the Wellington fault is not in the low slip rate category, so having it characterised between the values expected for high and low slip rate faults is likely to be appropriate.

4.2 Modelling methodologies

A method to compute the seismic radiation from a rupture of a large, complex fault, whose slip history has been determined by the synthetic seismicity algorithm described in the previous section, must take into account the following:

- The total radiation is the synthesis of the radiation of many subfaults, each with its own values of horizontal and vertical slips i.e. multiple slip events are allowed for each subfault of the main fault during the whole rupture process. The Coulomb failure criterion is applied to each subfault by considering both static and dynamic friction. This will determine the slip history and variable rise time for each subfault;
- Each subfault can break many times during the rupture process;
- The subfault size is small as compared with the whole rupture area, but not as small so as to represent its radiation by that of a point source, neglecting its directivity, particularly when the observation point is close to the fault;
- The main fault is embedded in a stratified medium with flat interfaces.

To that effect, we consider two possibilities. In the first, each subfault is a rectangular fault of length L and width W , rupturing with the rupture velocity prescribed in the synthetic seismicity algorithm. In the second, each subfault is represented by a point source at its centre, and its directivity incorporated by correction factors for P and S waves, each time it breaks. In both cases we assume that the main fault is embedded in a stratified medium with flat interfaces, and the seismic wave propagation through the layers is performed by means of generalised reflection-transmission coefficients (Kennett, 1983).

4.2.1 Implementation of the finite fault approach at subfault level

Referring to Figure 5, the main fault is discretised into many rectangular faults, each of length L and width W . The seismic radiation from each of them is computed by the Haskell model (Haskell, 1964) for propagating ruptures, assuming an elastic full-space whose parameters are those of the layer containing the fault in a stratified medium with flat interfaces. The idea is



that we formulate the mathematical expression of the total wavefield from all contributing subfaults, at each step of time, as if the other layers do not exist, and incorporate the layering by assuming that the main fault is fully contained in one layer. To propagate the wavefield through the other layers by using the generalised reflection-transmission coefficients we need only to compute it at the top and bottom interfaces of this layer.

Following the discrete wave number representation of the Haskell model (Bouchon, 1979; Chin & Aki, 1991; Chin, 1992), the radiated seismic wavefield from one subfault can be derived from the potentials:

$$\phi = \frac{\mu S}{F} \int_0^L \int_0^W \left(\frac{\partial \phi^3}{\partial x_1} + \frac{\partial \phi^1}{\partial x_3} \right) \exp(-i\omega x_1/v_r) dx_1 dx_2 \quad (1)$$

$$\vec{\psi} = \frac{\mu S}{F} \int_0^L \int_0^W \left(\frac{\partial \vec{\psi}^3}{\partial x_1} + \frac{\partial \vec{\psi}^1}{\partial x_3} \right) \exp(-i\omega x_1/v_r) dx_1 dx_2$$

where x_1, x_2 , and x_3 are local cartesian coordinates attached to the fault plane (x_3 being perpendicular to the fault plane).

In equations (1) ϕ is dilatational potential, $\vec{\psi}$ is shear vector potential, and v_r is rupture velocity. S is slip and μ rigidity, so that $\mu S dx_1 dx_2$ is the seismic moment of the double-couple element. The quantities $\phi^1, \phi^3, \vec{\psi}^1, \vec{\psi}^3$ are the potentials due to single forces of strength F applied along the x_1 and x_3 directions, respectively, expressed as Fourier superposition of plane waves, and assuming dependency on time of the form $\exp(-i\omega t)$, where ω is the circular frequency $2\pi f$, with f frequency. These expressions are rotated into the geographical coordinates X (North), Y (East) and Z (vertical -positive down), and the integration $\int_0^L \int_0^W$ carried out over each plane wave component defined by the wavenumbers k_x and k_y .

In the geographical coordinates, the displacement vector can be written as $\vec{U} = (u_x, u_y, u_z) = \nabla \phi + \nabla \times (\psi_1, \psi_2, \psi_3) = \nabla \phi + \frac{1}{ik} \nabla \times \nabla \times (0, 0, \psi_{SV}) + \nabla \times (0, 0, \psi_{SH})$ in the plane of incidence defined by $k = (k_x^2 + k_y^2)^{1/2}$, with $\psi_{SV} = \frac{k_x}{k} \psi_2 - \frac{k_y}{k} \psi_1$ and $\psi_{SH} = \psi_3 - \text{sgn}(z) \frac{\gamma}{k^2} (k_x \psi_1 + k_y \psi_2)$, where the quantities $\nu = (\omega^2/\alpha^2 - k^2)^{1/2}$ and $\gamma = (\omega^2/\beta^2 - k^2)^{1/2}$ are vertical wavenumbers for P and S waves, respectively. α and β are the velocities of the P and S waves, respectively.

The superposition is computed upon discretization of the wavenumbers k_x and k_y over the range $2\pi/L_x, 2\pi/L_y$, where L_x and L_y are distances along X and Y, respectively. For each Fourier component (k_x, k_y) :



$$\phi^\pm(k_x, k_y) = R_P^\pm \exp[-ik_x(x - x_r) - ik_y(y - y_r) \pm i\nu(z - z_r)] \quad (2)$$

$$\psi_{SV}^\pm(k_x, k_y) = R_{SV}^\pm \exp[-ik_x(x - x_r) - ik_y(y - y_r) \pm i\gamma(z - z_r)]$$

$$\psi_{SH}^\pm(k_x, k_y) = R_{SH}^\pm \exp[-ik_x(x - x_r) - ik_y(y - y_r) \pm i\gamma(z - z_r)]$$

were \pm refers to waves going up (+) and down (-) in the fault layer, and (x_r, y_r) are the X-Y coordinates of the point of the subfault where the rupture starts. The coefficients R_P^\pm , R_{SV}^\pm and R_{SH}^\pm pertain to the radiation of P , SV and SH wavefields in the geographical coordinates (after carrying out the integration $\int_0^L \int_0^W$), and include the values of moment tensor and the geometrical parameters defining the subfault, as well as the directivity. The exact expressions of these coefficients are given in the Appendix.

The potentials in (2) represent the (k_x, k_y) component of the seismic wavefield contribution of one subfault and for a single frequency. Our concern, as stated at the beginning of this section, is the seismic radiation during at least the rupturing time of many subfaults, each of which can, in turn, break many times, plus the time of wave propagation from the latest rupture to an observation point. A convenient way to elaborate an algorithm that takes into account these conditions is by assuming that the whole rupture process takes place in N time steps, and that in each time step there are N_r ruptures, regardless of which subfaults broke in the previous time step. In this sense, the number of subfaults becomes irrelevant. Since the potentials (2) are scalar quantities, the (k_x, k_y) component of the wavefield due to the $N \times N_r$ subfault ruptures can be expressed as:

$$\Phi^\pm(k_x, k_y) = \sum_{n=1}^N \left\{ \sum_{m=1}^{N_r} \phi_{nm}^\pm(k_x, k_y) \right\} \exp(-i\omega t_n) \quad (3)$$

$$\Psi^\pm(k_x, k_y) = \sum_{n=1}^N \left\{ \sum_{m=1}^{N_r} \psi_{nm}^\pm(k_x, k_y) \right\} \exp(-i\omega t_n)$$

where t_n is the time shift corresponding to the time step n . Ψ^\pm and ψ_{nm}^\pm hold for either SV or SH waves. These are properly computed by using (2).



Once the potentials (3) have been calculated, the displacement and stress wave-fields in the source layer L can be computed from:

$$\begin{pmatrix} u_x \\ u_z \\ \tau_{zx} \\ \tau_{zz} \end{pmatrix} = \begin{pmatrix} -ik & i\gamma_L & -ik & -i\gamma_L \\ -i\nu_L & -ik & i\nu_L & -ik \\ -2\mu_L\nu_L k & -\mu_L l_L & 2\mu_L\nu_L k & -\mu_L l_L \\ \mu_L l_L & -2\mu_L\gamma_L k & \mu_L l_L & 2\mu_L\gamma_L k \end{pmatrix} \begin{pmatrix} \Phi^- \\ \Psi_{SV}^- \\ \Phi^+ \\ \Psi_{SV}^+ \end{pmatrix} \quad (4)$$

for $P - SV$ waves; and

$$\begin{pmatrix} u_y \\ \tau_{zy} \end{pmatrix} = \begin{pmatrix} -ik & ik \\ \mu_L\gamma_L k & -\mu_L\gamma_L k \end{pmatrix} \begin{pmatrix} \Psi_{SH}^- \\ \Psi_{SH}^+ \end{pmatrix} \quad (5)$$

for SH waves, where:

$$\begin{aligned} k &= (k_x^2 + k_y^2)^{1/2} \\ \nu_L &= (\omega^2/\alpha_L^2 - k^2)^{1/2} \\ \gamma_L &= (\omega^2/\beta_L^2 - k^2)^{1/2} \\ l_L &= (2k^2 - \omega^2/\beta_L^2)^{1/2} \end{aligned}$$

4.2.1.1 Results

The case addressed in this work pertains to a M7.4–7.5 earthquake on the Wellington fault, whose slip history has been determined by a synthetic seismicity algorithm based on multiple fault patch interactions (Robinson & Benites, 1995, 1996 & 2001) described in the previous section. The Wellington fault is represented by a strike-slip, vertical, rectangular fault 75 km long and 20 km wide, embedded in the second layer of the horizontally layered structure given in Table 3. The strike of the fault is oriented along Y (East). The fault is discretised into 75×20 subfaults, i.e. each subfault is an square of 1 km² area. For 1 metre slip and a rigidity value $\mu=2.67\times 10^{10}$ Newton/m², this subfault would produce an event of M4.9. The initiation point, i.e. the first subfault that breaks, is not prescribed *a priori*, but is determined by the synthetic seismicity algorithm.



The values of the slip history enter the computer program that calculates seismograms as follows:

$$\begin{array}{l} t_n \quad m \\ y_{n1} \quad x_{n1} \quad z_{n1} \quad s1_{n1} \quad s2_{n1} \\ y_{n2} \quad x_{n2} \quad z_{n2} \quad s1_{n2} \quad s2_{n2} \\ \cdot \\ \cdot \\ y_{nm} \quad x_{nm} \quad z_{nm} \quad s1_{nm} \quad s2_{nm} \\ t_{n+1} \\ \cdot \end{array}$$

where t_n is the n^{th} rupture time step, m is the number of subfault ruptures in that time step, y_{nm} , x_{nm} , and z_{nm} are the geographical coordinates of the subfault having the nm^{th} rupture, and $s1_{nm}$ and $s2_{nm}$ are the slip values along strike and down dip, respectively, of the m^{th} rupture. In our case, for a $M7.5$ earthquake, the whole rupture is composed of 2284 time steps, totalling 50,000 subfault ruptures with slip values ranging from tenths of a metre to just under 1 metre.

The assumption of harmonic dependence, $\exp(-i\omega t)$, is equivalent to Fourier transforming the solutions of the wave equation from the time domain to frequency domain. Given the large number of ruptures in our case, this is convenient in two ways. First, time domain seismograms can be constructed by the synthesis of the solutions for many frequencies in the frequency range prescribed for the problem. The synthesis is done by convolution with an appropriate source-time function describing the slip episode on the subfault. Second, each frequency solution can be calculated independently by a node of a cluster of computers arranged for parallel processing. A seismogram of T seconds duration sampled with N_T points can be computed with $N_T/2$ frequency points for maximum frequency $N_T/2T$. We can, as well, split the total number of ruptures into groups of several rupture time steps and send each to be computed independently by a node of a cluster of computers. The results from all nodes can be superimposed in the frequency domain in a simple manner.

We have followed the last option, and split the 50000 ruptures into 20 groups of 2500 ruptures each, and sent each group to be computed by a node of "Terremoto", a parallel computer built at GNS. This is a cluster of 21 PC's (AMD Athlon 1.2 GHz with 768 MB RAM each), interconnected with fast ethernet. We choose a station location near the fault (Site 1 in Fig. 1), specifically at $x=5$ km (distance from the fault measured to the northwest) and $y=65$ km (distance along the fault measured from the southwest end) and used the slip time history from Event 1 as input (Fig. 3). Event 1 initiates near to the northeastern end of the fault, so Site 1 is very near to the rupture initiation point. Figure 6 shows the synthetic seismograms for a duration of 50 s, from left to right, for components perpendicular to the fault (U), parallel to the fault (V) and vertical (W), and for displacement (first row), velocity (second row) and acceleration (third row). The displacement spectra are shown at the bottom, for each component, computed for a 48 s time window. The maximum frequency is 10.24 Hz, sampled by 512 points (1024 time points). We have used a modulated ramp function (Ben-



Menahem and Singh, 1981, Table 4.9, p. 240) as the source time function for each rupture. The non-causal “ringing” shown here and in some of the seismograms hereafter is due to aliasing caused by using a 0.1 s rise time for the ramp.

The peak values of displacement in Figure 6 are about as expected for a $M7.4$ earthquake when compared to data from sites close to large crustal earthquakes world-wide (Table 7). In Figure 6, peak values are generally in the 20–30 cm range, except for a high value of 50 cm with an arrival time of about 16 s on the vertical component. This high value is most likely due to radiation from the largest asperity (Fig. 3). High values of displacement seen in world-wide data (up to 255 cm) are most likely due to static fault offsets (“fault fling”). In our synthetics the static terms are included in the solution, but have been tapered out of the seismograms in post-processing because they are so dominant at close distances.

Peak values for velocity are generally in the 200–300 cm/s range. These too compare quite favourably with world-wide data. Again the vertical component shows a high value (~350 cm/s) at 16 s, likely to be due to the large asperity.

Peak accelerations are generally in the range 1.4–2.4g. Values exceeding 2g have been observed occasionally (Table 7), but are most likely to be recorded at hard rock sites. In this regard, it needs to be noted that our model has no superficial soft rock layers ($V_s = 2.54$ km/s for our top layer), nor has attenuation of the type $\exp(-\omega r/2vQ)$ incorporated, where r is the distance, v is either the P or S wave velocity, and Q the “quality” factor for propagation. The values we have calculated are thus not surprisingly high and would reduce significantly once superficial layers of softer rock were included, along with appropriate frequency dependent attenuation terms. The inclusion of these terms would have less effect on the velocity and displacement values than on the acceleration, because the acceleration amplitudes are weighted by a factor of ω^2 . We have assumed a harmonic time dependency of the displacement, i.e. of the form $e^{-i\omega t}$. The amplitudes of the velocity and acceleration will be weighted by factors of ω and ω^2 , respectively. Further attenuation of large accelerations would come from the non-linear behaviour of surface soil layers in basins, which can be treated locally at the observation point.

Figures 7 and 8 show the high-pass filtered seismograms (top) and corresponding displacement spectra (bottom), high-pass filtered at 1 Hz and 2 Hz, respectively. These plots show the changing nature of the seismograms at different frequencies, with the higher frequencies being predominant in the earlier stages of the rupture at Site 1 when the rupture front is closest to the site.

Figure 9 shows displacement, velocity, and acceleration seismograms and displacement spectra for the same Event 1 rupture discussed above, but recorded at Site 2 at the southwestern end of the fault (Fig. 1). As expected, the fault-normal displacement seismogram shows a large low-frequency directivity pulse typical of a strike-slip fault breaking in the direction of the station. This is also prominent in the displacement spectra. Note that the directivity pulse is less prominent in the velocity and acceleration seismograms



where higher frequencies dominate. Again this is the behaviour expected from world-wide data because directivity tends to break down at higher frequencies (Somerville *et al.*, 1997).

Figure 9 also shows late-arriving (45–50 s) high-frequency energy, especially on the vertical component seismograms. This energy is most likely generated by slip on a large, nearby asperity. This could be confirmed by running simulations with the predominant asperities separated out into separate ruptures.

The displacement spectra show that the largest amplitude values for the three components occurs between about 0.4 Hz and at 3 Hz. At 3.5 Hz there is a sharp drop of amplitude of nearly two orders of magnitude for all three components. It is difficult to analyse this sharp decrease in terms of the subfault corner frequency or stopping phase, strictly defined for body waves, because in this case the wave field is the superposition of *P* and *S* body waves all combined with surface waves. Taking into account that the dimension of a subfault is 1 km, and that the rupture velocity is 3.46 m/s, we believe that the sharp drop of spectral amplitude is the result of an artefact, related to the inverse of the time (1/3.46 s) that it takes the rupture to travel across the subfault. This sharp drop can also be observed at Site 2 (Fig. 9).

The drop in spectral amplitude related to the size of the subfault might be a serious disadvantage to representing the seismic radiation of a complex rupture as the superposition of the radiation from multiple ruptures of rectangular subfaults. The effect can be reduced by decreasing the size of the subfaults, but this will impose higher computational cost to both the synthetic seismicity and seismic radiation algorithms. In fact, the synthetic seismicity algorithm computes the values of the overall static stress tensor at the centre of each subfault, where the Coulomb stress failure criterion is applied. The slip values, therefore, correspond more to a point rather than to an extended area of the subfault. Taking into account that the slip values can vary by several orders of magnitude from one time step to the next, and for subfaults next to each other, assigning the slip values to the area of the subfault will make the discretisation unrealistically heterogeneous, since the slip contrast at the edges of the subfaults are not constrained by boundary conditions. For this reason, we believe it appropriate to develop a model to compute the seismic radiation of the main rupture based on a double-couple point source distribution.

4.2.2 Implementation of the point source with directivity model

In this approach a double-couple point source is located at the centre of the rectangle representing the subfault. This can be justified by the fact that in most cases of interest the size of the subfault will be much smaller than the distance to the observation point, but not so small as to neglect the effects of directivity. The formulation in this case is similar to the one in the previous section, i.e., by assuming that the main fault is totally embedded in one layer, the seismic radiation can be constructed from the wave contributions of all the point sources radiating in one time step. The potentials for a double-couple point source are :



$$\begin{aligned}\phi^\pm(k) &= R_P^\pm \exp[\pm i\nu(z - z_r)] \\ \psi_{SV}^\pm(k) &= R_{SV}^\pm \exp[\pm i\gamma(z - z_r)] \\ \psi_{SH}^\pm(k) &= R_{SH}^\pm \exp[\pm i\gamma(z - z_r)]\end{aligned}\tag{6}$$

where $k = (k_x^2 + k_y^2)^{1/2}$, and R_P^\pm , R_{SV}^\pm , and R_{SH}^\pm , the radiation coefficients for P , SV and SH waves, are given in the Appendix. These coefficients already incorporate the X-Y dependence of the radiation pattern analytically, thanks to the azimuthal symmetry of the point source, in terms of Bessel functions of zero and first orders $J_0(kr)$ and $J_1(kr)$, respectively, with $r = [(x - x_r)^2 + (y - y_r)^2]^{1/2}$ the radial distance to any point (x, y) in X-Y, and $k = (k_x^2 + k_y^2)^{1/2}$. This is because the term $\exp[-ik_x(x - x_r) - ik_y(y - y_r)]$ (see e.g. equation 2) determining the wave propagation in the plane X-Y can be reduced to $\exp(-ikr \cos \varphi)$ by considering $k_x = k \sin(\varphi)$, and $k_y = k \cos \varphi$, with φ the angle between r and k . The double integration on k_x and k_y is then transformed into a double integration on k and φ . Since the full azimuthal wavenumber coverage is for φ varying from 0 to 2π , the integrals containing $\exp(-ikr \cos \varphi)$ will yield the Bessel functions (Chin and Aki, 1991).

Other symbols and quantities in (6) are defined as in (2).

$$\begin{aligned}\Phi^\pm(k_x, k_y) &= \sum_{n=1}^N \left\{ \sum_{m=1}^{N_r} \phi_{nm}^\pm(k_x, k_y) \frac{\sin X_{Pm}}{X_{Pm}} \right\} \exp(-i\omega t_n) \\ \Psi^\pm(k_x, k_y) &= \sum_{n=1}^N \left\{ \sum_{m=1}^{N_r} \psi_{nm}^\pm(k_x, k_y) \frac{\sin X_{Sm}}{X_{Sm}} \right\} \exp(-i\omega t_n)\end{aligned}\tag{7}$$

in which X_P and X_S are the directivity correction factors for P and S waves, respectively, applied to each subfault, defined by :

$$X_P = \frac{\omega L}{2v_p} (v_p/v_r - \cos \theta)$$

$$X_S = \frac{\omega L}{2v_s} (v_s/v_r - \cos \theta)$$



with v_r = average rupture velocity, and θ the angle between the point source corresponding to the rupture m and the station. The components of the wavefield contribution of each subfault in the k - z plane are rotated to the geographical coordinates. Other symbols and quantities in (6) are defined as in (2).

4.2.2.1 Results

Figure 10 shows the results from the point source summation approach, with a directivity correction, for Event 1 as recorded at Site 1 (northeastern end of fault). A comparison of the spectral plots shows that the high amplitude of frequencies between 2 and 3.5 Hz, thought to be an artefact related to subfault size and subfault rupture velocity in the finite fault simulations (Fig. 6), have now been reduced by at least an order of magnitude. Also noticeable is the extension of relatively high frequencies out to nearly 10 Hz, with a very rapid falloff after that. This is probably due to the effect of the small rise-time (0.1 s) used as the source time function for each rupture. When this value is 0.5 s the falloff occurs between 2–3 Hz (Fig. 11). Strictly speaking, the rectangular fault smoothes the higher frequencies more than the point source because its radiation pattern contains two “sinc” functions in terms of length L and width W (see Appendix), instead of just one in the point source case.

On the seismogram plots in Figure 10, displacements are a little less than for the finite fault case. The large long-period signal on the fault-parallel displacement seismogram is most likely an artefact created during the removal of a large static offset. Such offsets are difficult to remove when the seismogram length has been limited to minimise computation time. Velocity amplitudes are very similar across the two simulations, while accelerations are a little higher for the point source simulation. As discussed earlier, the incorporation of low-velocity surface layers with realistic attenuation values would significantly reduce the accelerations.

The seismogram plots also show significant differences in the shape of the waveform envelope. We had expected that envelope shape would be quite strongly influenced by the slip time history and propagation, and thus not vary much with the method of subfault calculation. This does not seem to be the case. Instead, it seems that the envelope shape is strongly influenced by the frequency content of the seismogram and this is dependent on the rise time that is used and the method of summation that is employed. Ideally, the rise time would be adjusted to match the frequency content across the finite fault and point source methods to compensate for the extra smoothing inherent in the finite fault approach.

Figure 12 shows the results from the point source with directivity correction summation for Event 1 as recorded at Site 2 (southwestern end of fault). A comparison of the spectral plots with those from the Site 1 summation (Fig. 10) shows a marked decrease in frequencies in the 2–10 Hz range. A similar effect can be seen between the respective finite fault simulations (Figs. 6 & 9), but it is less marked in that case. We would expect Site 2 to experience a boost



in low frequencies on the fault-normal component, but these data are showing fewer high frequencies across all components.

A further feature in Figure 12 is the strong directivity pulse on the fault-normal component. This has a greater amplitude in terms of displacement than in the finite fault case. This may be due to constructive interference being stronger for the point source simulation — related to subfault size and the speed with which the rupture front is propagating. A fault-normal arrival persists on the velocity and acceleration seismograms that is a little larger than for the finite fault example (Fig. 9; note the different amplitude scales). This arrival is larger because again the point source simulation has more high frequencies present than the finite fault simulation. Normally we expect the directivity pulse to “wash out” at higher frequencies due to the breakdown of radiation pattern and the less coherent summation of energy in the rupture direction. This effect could be explicitly added to our models, if necessary, but it is already incorporated to some degree by the randomness inherent in the input slip time history.

Figure 13 shows the results from the point source with directivity correction summation for Event 2 as recorded at Site 1 (northeastern end of fault). Recall that Event 2 is a predominantly bilateral rupture, so its directivity properties will differ from Event 1 for the receiver sites that we are considering. A comparison of the spectral plots with those from the Event 1 summation (Fig. 10) shows quite close similarities. There are, however, significant differences in the time domain. First, note that the large long-period signals on the displacement seismograms are most likely an artefact created during the removal of a large static offset and should be ignored. There is a strong arrival on all fault-normal components at about 25–30 s. We interpret this to be energy arriving from the closest asperity, which generates very high peak accelerations. There may also be a residual fault-normal directivity effect. If this is the case, it may need to be “washed out” by the inclusion of appropriate frequency dependent terms in the calculations, as discussed above. This, along with the incorporation of softer rock and attenuation, would significantly reduce the peak accelerations. Other amplitudes agree well with our earlier simulations. Also note that, due to the bilateral rupture process, the overall duration of rupture is less than for Event 1.

Finally we present the results from the point source with directivity correction summation for Event 2 as recorded at Site 2 (southwestern end of fault) in Figure 14. The spectral shape for this simulation lies between what we have observed for Event 1 at this site (Fig. 12) and those for Site 2 (Figs. 10 & 13). Note that, given we are using a uniform horizontally layered velocity structure, we do not expect any site-specific amplification of shaking. Any spectral features that persist at a site must be due to the site’s position relative to the rupture. As in the previous simulation, the displacement seismograms exhibit some artefacts related to the removal of static offsets. A prominent pulse is again apparent, in this case corresponding to rupture of the prominent asperity at the southwestern end of the fault. Here the rupture energy arrives over a very short duration (clearer in the fault-parallel velocity and acceleration seismograms in Fig. 14). The most likely reason for this is that the arrival of energy from the two largest asperities is nearly coincident, although that could only be confirmed by running simulations containing a single asperity at a time.



5.0 SUMMARY AND CONCLUSIONS

We have defined a 3-segment fault model for the Wellington fault based on geological evidence and the fault geometry. The model has a 75 km length, a 20 km width, and dips at 80° to the northwest. Purely horizontal dextral faulting has been assumed. Scaling relations suggest a likely magnitude of M_w 7.4–7.6.

We have modelled a smooth rupture across the fault and generated synthetic seismograms for two near-fault sites. In our original proposal, it had been our intention to compare the smooth ruptures with both EGF summations (Pancha *et al.*, 2002) and more complex ruptures. At an early stage, however, it was realised that a smooth rupture cannot generate the high frequencies that are contained in either EGF or complex rupture models. Furthermore, the EGF summation has no inherent low frequency motions (these are artificially added), so there is no overlap of frequencies for which valid comparisons could be made.

Smooth rupture models can be used to test the effect of fault geometry, however. Tests of this type showed that a 3-segment model gave noticeably different low frequency seismograms for near-fault stations. We have interpreted this as being due to changes in station location with respect to the radiation pattern from various parts of the fault as the rupture propagates past. It also highlights the need to use accurate fault geometry and site locations to in turn generate reliable seismograms.

We have used synthetic seismicity models, based on the interaction between many fault patches, or subfaults, to generate detailed slip distributions for ruptures over the model fault plane. We have shown that these slip distributions are consistent with relations derived from large global earthquakes, particularly in terms of size and distribution of asperities.

In our original proposal, our intent was to treat each subfault in the synthetic seismicity model as a small finite fault, compute the radiation from that fault, and then sum over all subfaults to produce synthetic seismograms. This has been achieved, but the approach has two shortcomings. First, the calculations are very computer intensive. The original coding was re-written to enhance the computational efficiency and then further modified to allow it to be implemented on a cluster of 21 PC's. It was found that even with these modifications, it required at least a week of computation to calculate the seismograms for a single site. While this makes obtaining some results possible, more rapid turn-around is required for more detailed study of the predicted ground shaking and what factors affect it. The second shortcoming was that displacement spectra are enhanced over the 2–3.5 Hz range and then show a sudden decrease at frequencies related to the subfault size. Artefacts of this kind are not unexpected, but given that they are nearly two orders of magnitude in size they are quite undesirable if the synthetic seismograms are to be of practical use. We believe that the artefact is related to the frequencies produced by the starting and stopping of the ruptures across each individual subfault.

As a more practical alternative to the finite fault approach, we have treated each subfault as a point source, but have included directivity through adding correction factors for the *P* and *S*



waves. This reduced computation times on the Terremoto cluster to about five hours, and also greatly reduced the artefact related to subfault size. This method, however, also seems to have some shortcomings. Waveforms and spectra differ significantly from the finite fault results. This is most likely to be due to the use of the same rise time as for the finite fault approach and can be remedied by adjusting the rise time so that the frequency content of the two approaches is matched (the finite fault approach having greater inherent smoothing than the point source approach).

Both methods of rupture summation produce displacement and velocity seismograms with peak amplitudes near to those expected, based on observations from global earthquakes. The only exceptions to this are the high accelerations due to very close asperities. The effect of asperities cannot be modelled deterministically because, with the current state of knowledge, we do not know where they are prior to a rupture. With the methodology that we have developed here we will be able to assess the impact of asperities for a variety of rupture scenarios. Our preliminary results are indicating that they will be very important for close stations at high frequencies. In general, peak accelerations tend to be a little high, but this is most likely to be due to using a model with high velocities (akin to very hard rock) near to the surface and the lack of any attenuation terms. A high priority for further work would be to improve the velocity model and to include the effects of attenuation.

The models correctly reproduce clear fault-normal directivity pulses at low frequencies. In future work we hope to examine these in detail to look at their behaviour for a range of earthquake magnitudes and to see when the breakdown in directivity is occurring as a function of frequency. Fault fling effects should also be present in the models as a static offset. In the current study these offsets have been filtered out. We have not yet fully developed ways to cleanly remove these effects because seismogram lengths have been limited to minimise computation time. The static offsets also deserve further investigation for near fault sites. In this regard, fault geometry will be important. The 3-segment fault geometry has not been explicitly included in our complex fault simulations, but it can be included by running the summation in separate parts and then adding the results. For the current project, difficulties experienced in getting an effective summation scheme working has meant that less time has been available to fully implement the 3-segment model.

In summary, we have succeeded in implementing two methods for summing subfault ruptures produced from a synthetic seismicity catalogue. We see this as a big step forward over other techniques that have had to rely on the synthesis of separate deterministic and stochastic approaches for low and high frequencies, respectively. Both of our summation methods give reasonable values for near-fault motions in terms of peak displacement, velocity, and acceleration and, when more fully developed, will lead to more insight into the generation of strong ground motions. Both approaches, however, have some shortcomings that need further work to overcome. The most significant of these, and perhaps the most easily overcome, are the use of lower velocity surface layers (softer rock), the inclusion of attenuation terms, and suitable matching of frequency content across the two approaches by adjusting rise time duration.



6.0 ACKNOWLEDGEMENTS

This work was largely funded by the EQC Research Foundation whose support is gratefully acknowledged. It was also partly supported by the Foundation for Research, Science, and Technology under contract C05XC0006. Carolyn Hume, Philip Carthew, Penny Murray and Sarah Taylor assisted with the report preparation.

7.0 REFERENCES

- Abercrombie, R.E. & R.A. Benites (1998). Strong motion modelling of the 1993 Tikokino earthquake, southern Hawke's Bay, New Zealand. *NZ J. Geol. & Geophys.*, 41, 259–270.
- Aki, K. & P. G. Richards (1980). Quantitative seismology theory and methods. W. H. Freeman & Company, San Francisco. 932p.
- Akkar, S. & P. Gulkan (2002). A critical examination of near-field accelerograms from the Sea of Marmara region earthquakes. *Bull. Seism. Soc. Am.*, 92, 428–447.
- Aoi, S, S. Haruko, I. Tomotaka & F. Hiroyuki (1998). Simulation of the 1995 Hyogoken-Nanbu earthquake with the 3-D fourth-order FDM using discontinuous grids. *Eos, Trans. Am. Geophys. Un.*, 79, F577.
- Ben-Menahem, A. & S. J. Singh (1981). Seismic waves and sources. Springer-Verlag, New York. 1108 p.
- Benites, R. A., K. B. Olsen & P. R. Wood (2000). Modeling strong ground motions in the Wellington Metropolitan area, New Zealand. *Eos, Trans. Am. Geophys. Un.* 81, F828.
- Berryman, K. (1990). Late Quaternary movement on the Wellington fault in the Upper Hutt area, New Zealand. *NZ J. Geol. Geophys.*, 33, 257–270.
- Bouchon, M. (1979). Discrete wavenumber representation of elastic wave fields in three-space dimensions. *J. Geophys. Res.*, 84, 3,609–3,614.
- Carter, L., K. B. Lewis & F. Davey (1988). Faults in the Cook Strait and their bearing on the structure of central New Zealand. *NZ J. Geol. Geophys.*, 31, 431–446.
- Chin, B. H. (1992). Simultaneous study of the source, path and site effects on strong ground motion during the 1989 Loma Prieta earthquake. Ph. D. Thesis, Univ. S. California.
- Chin, B. H. & K. Aki (1991). Simultaneous study of the source, path and site effects on strong ground motion during the 1989 Loma Prieta earthquake: a preliminary result on pervasive non-linear site effects. *Bull. Seism. Soc. Am.*, 81, 1,859–1,884.
- Dan, K. and Sato, T. (1999) A semi-empirical method for simulating strong ground motion based on variable-slip rupture models for large earthquakes, *Bull. Seism. Soc. Am.*, 89, 36–53.



- Dan, K. T., Watanabe, T., Tanaka, T., and Sato, R. (1990) Stability of earthquake ground motion synthesized by using different small-event records as empirical Green's function, *Bull. Seism. Soc. Am.*, 80, 1,433–1,455.
- Darby, D. & J. Beavan (2002). Evidence from GPS measurements for contemporary interplate coupling on the southern Hikurangi subduction thrust and for partitioning of strain in the upper plate. *J. Geophys. Res.* (In press).
- Day, S.M. (1998) Efficient simulation of constant Q using coarse-grained memory variables, *Bull. Seism. Soc. Am.*, 88, 1051–1062.
- Frankel, A. (1995). Simulating strong motions of large earthquakes using recordings of small earthquakes: the Loma Prieta mainshock as a test case. *Bull. Seism. Soc. Am.*, 85, 1144–1160.
- Hall, J. F., T. H. Heaton, M. W. Halling & D. J. Wald (1995). Near-source ground motion and its effects on flexible buildings. *Earthquake Spectra*, 11, 569–605.
- Hanks, T. C. & W. H. Bakun (2002). Source-scaling models for M-log A observations of continental earthquakes. *Bull. Seism. Soc. Am.*, (in press).
- Hartzel, S. (1978). Earthquake aftershocks as Green's functions. *Geophys. Res. Lett.*, 5, 1–4.
- Haskell, N. A. (1964). Radiation pattern of surface waves from point sources in a multi-layered medium. *Bull. Seism. Soc. Am.*, 54, 377–394.
- Heaton, T. H. (1990). Evidence for and implications of self-healing pulses of slip in earthquake rupture. *Phys. Earth Planet. Int.*, 64, 1–20.
- Heaton, T. H., J. F. Hall, D.J. Wald & M. N. Halling (1995). Response of high-rise and base-isolated buildings to hypothetical Mw7.0 blind thrust earthquake. *Science*, 267, 206–211.
- Irikura, K. (1983) Semi-empirical estimation of strong ground motions during large earthquakes, *Bull. Disas. Prev. Inst. Kyoto Univ.* 33, Part 2 No. 298, 63–104.
- Irikura, K. (1986) Prediction of strong acceleration motions using empirical Green's function, *Proc. 7th Jap. Earthquake Eng. Symp.* 151-156.
- Joyner, W.B. and Boore, D.M. (1988) Measurement, characterization, and prediction of strong ground motion, *Earthquake Eng. Soil Dyn. II, Recent Advances in ground-motion evaluation*, ASCE, 43-102.
- Kamae, K., K. Irikura & A. Pitarka (1998). A technique for simulating strong ground motion using hybrid Green's function. *Bull. Seism. Soc. Am.*, 88, 357–367.
- Kanamori, H. (1979) A semi-empirical approach to prediction of long-period ground motion from great earthquakes, *Bull. Seism. Soc. Am.* 69, 1645-1670.
- Kennett, B. L. N. (1983). *Seismic wave propagation in stratified media*. Cambridge, Cambridge University Press, U.K.



- McGuire, J. J., L. Zhao, & T. H. Jordan (2002). Predominance of unilateral rupture for a global catalogue of large earthquakes. *Bull. Seism. Soc. Am.* (submitted).
- Pancha, A., M.P. Chadwick & T.H. Webb (2002). Rupture simulation on the Wellington fault using an empirical Green's function analysis (In prep.)
- Reyners, M., R. Robinson & P. McGinty. Plate coupling in the northern South Island and southernmost North Island, New Zealand, as illuminated by earthquake focal mechanisms. *J. Geophys. Res.*, 102, 15,197–15,210.
- Rhoades, D. A., R. J. Van Dissen & D. J. Dowrick (1994). On the handling of uncertainties in estimating the hazard of rupture on a fault segment. *J. Geophys. Res.*, 99, 13,701–13,712.
- Robinson, R. (1986). Seismicity, structure and tectonics of the Wellington region, New Zealand. *Geophys. J. R. Astr. Soc.*, 87, 379–409.
- Robinson, R. & R. Benites (1995). Synthetic seismicity models for multiple interacting faults. *J. Geophys. Res.*, 100, 18,229–18,238.
- Robinson, R. & R. Benites (1996). Synthetic seismicity models for the Wellington region, New Zealand: Implications for the temporal distribution of large events. *J. Geophys. Res.*, 101, 27,833–27,844.
- Robinson, R. & R. A. Benites (2001). Upgrading a synthetic seismicity model for more realistic fault ruptures. *Geophys. Res. Lett.*, 28, 1843–1846.
- Somerville, P., K. Irikura, R. Graves, S. Sawada, D. Wald, N. Abrahamson, Y. Iwasaki, T. Kagawa, N. Smith & A. Kowada (1999). Characterizing crustal earthquake slip models for the prediction of strong ground motion. *Seis. Res. Lett.*, 70, 59–80.
- Somerville, P. G., Sen, M., and Cohee, B. (1991) Simulation of strong ground motions recorded during the 1985 Michoacan, Mexico and Valparaiso, Chile earthquakes, *Bull. Seism. Soc. Am.* 81, 1-27.
- Somerville, P. G., N. F. Smith, R. W. Graves, & N. A. Abrahamson (1997). Modification of empirical strong ground motion attenuation relations to include the amplitude and duration effects of rupture directivity. *Seis. Res. Lett.*, 68, 199–222.
- Stirling, M. W., S. G. Wesnousky & K. Shimazaki (1996). Fault trace complexity, cumulative slip, and the shape of the magnitude-frequency distribution for strike-slip faults; a global survey. *Geophys. J. Int.*, 124, 833–868.
- Van Dissen, R. J., K. R. Berryman, J. R. Pettinga & N. L. Hill (1992). Paleoseismicity of the Wellington – Hutt Valley Segment of the Wellington fault, North Island, New Zealand. *NZ J. Geol. Geophys.*, 35, 165–176.
- Wald, D. J. (1996). Slip history of the 1995 Kobe, Japan, earthquake determined from strong motion, teleseismic, and geodetic data. *J. Phys. Earth*, 44, 489–503.



- Wald, D. J., R. W. Graves & V. Quitoriano (1996a). Finite-fault, 3D finite difference modelling of the Landers earthquake: studying the importance of rupture heterogeneity and the response of the Los Angeles basin for simulated and recorded ground motions. *Eos, Trans. Am. Geophys. Un.*, 77, F497.
- Wald, D. J., T. H. Heaton & K. W. Hudnut (1996b). The slip history of the 1994 Northridge, California earthquake determined from strong-motion, teleseismic, GPS and levelling data. *Bull. Seism. Soc. Am.*, 86, S49–S70.
- Webb, T. H., P. G. Somerville, D. I. Doser, D. L. Rhoades & A. Pancha (1998). Moment-area scaling of crustal earthquakes in New Zealand. *GNS client report* 45 pp.
- Wu, Y.-M., T.-C. Shin & C.-H. Chang (2001). Near real-time mapping of peak ground acceleration and peak ground velocity following a strong earthquake. *Bull. Seism. Soc. Am.* 91, 1218–1228.



Table 1 Wellington fault segment parameters

Segment	Length (km)	Width (km)	Strike (°)	Dip (°NW)	Rake (°)
Unsegmented	75.00	20	50	90	180
1	11.5	20	71	90	180
2	23.3	20	41	90	180
3	40.2	20	55	90	180

Table 2 Robinson (1986) velocity model for the Wellington Region

Thickness (km)	P velocity (km/s)	S velocity (km/s)
0.4	4.40	2.54
4.6	5.63	3.16
10.0	5.77	3.49
10.0	6.39	3.50
10.0	6.79	3.92
10.0	8.07	4.80
Halfspace	8.77	4.86

Table 3 Velocity model used in this study

Thickness (km)	P velocity (km/s)	S velocity (km/s)
0.4	4.40	2.54
20.0	5.95	3.43
12.6	6.71	3.85
10.0	8.07	4.80
Halfspace	8.77	4.86

Table 4 Input parameters for the synthetic seismicity model

Parameter	Value
Fault Length	75 km
Fault Width	20 km
Fault dip	90°
Coefficient of friction (background)	Random between 0.4–0.7
Coefficient of friction (asperities)	Random between 0.65–0.95
Stress drop	25%
Dynamic enhancement factor ¹	1.20
Pore pressure	Hydrostatic

¹see Robinson & Benites (2001)



Table 5 Comparison of output parameters from the synthetic seismicity slip model for Event 1 with those from world-wide regressions for an event with $M_o = 1.41 \times 10^{20}$ N-m (Mw7.40)

Parameter	Observed in our model	Predicted
Rupture area	1,500 km ²	2,810 km ²
Average slip	2.35 m	1.75 m
Area of asperities	345 km ²	629 km ²
Area of largest asperity	272 km ²	458 km ²
Radius of largest asperity	9 km	12.1 km
Number of asperities	2 (+1 very small)	2.6
Area covered by asperities	23%	22%
Average asperity slip contrast	1.67	2.01
Slip duration	3.00 s	2.28 s
Along-strike corner spatial wavenumber	0.010 km ⁻¹	0.011 km ⁻¹
Along-dip corner spatial wavenumber	0.010 km ⁻¹	0.028 km ⁻¹
Rupture duration (95% of slip)	30 s	

Table 6 Comparison of output parameters from the synthetic seismicity slip model for Event 2 with those from world-wide regressions for an event with $M_o = 1.92 \times 10^{20}$ N-m (Mw7.49)

Parameter	Observed in our model	Predicted
Rupture area	1,500 km ²	3,450 km ²
Average slip	3.20 m	1.94 m
Area of asperities	219 km ²	773 km ²
Area of largest asperity	121 km ²	563 km ²
Radius of largest asperity	11 km	13.4 km
Number of asperities	2 (+1 very small)	2.6
Area covered by asperities	16%	22%
Average asperity slip contrast	1.8	2.01
Slip duration	3.00 s	2.52 s
Along-strike corner spatial wavenumber	0.005 km ⁻¹	0.001 km ⁻¹
Along-dip corner spatial wavenumber	0.010 km ⁻¹	0.016 km ⁻¹
Rupture duration (95% of slip)	20 s	

Table 7 Range of peak near-source ground motions from large earthquakes

Earthquake	M _w	Distance (km)	Acceleration (g)	Velocity (cm/s)	Displacement (cm)
¹ 1971 San Fernando, USA	6.7	0	1.12	113	38
¹ 1978 Tabas, Iran	7.4	3	0.92	125	106
¹ 1979 Imperial Valley, USA	6.5	1-4	0.56-1.74	44-110	15-55
¹ 1985 Nahanni, Canada	6.8	0	0.50->2.00	31-39	31-36
¹ 1987 Superstition, USA	6.6	0-6	0.53-0.91	44-138	15-60
¹ 1989 Loma Prieta, USA	6.9	0-5	0.44-0.62	102-120	32-40
¹ 1992 Erzincan, Turkey	6.8	2	0.50	105	40
¹ 1992 Petrolia, USA	7.0	0-5	0.69->1.8	90-126	31-67
¹ 1993 Landers, USA	7.2	1	0.90	142	255
¹ 1994 Northridge, USA	6.7	0-5	0.32-1.82	44-177	13-50
¹ 1995 Kobe, Japan	6.9	0	0.31-0.85	55-176	18-26
² 1999 Chi-Chi, Taiwan	7.7	0-5	0.26-1.02	60-280	
³ 1999 Izmit, Turkey	7.6	3-4	0.17-0.41	14-85	11-199

¹Hall *et al.* (1995)

²Wu *et al.* (2001)

³Akkar & Gulkan (2002)

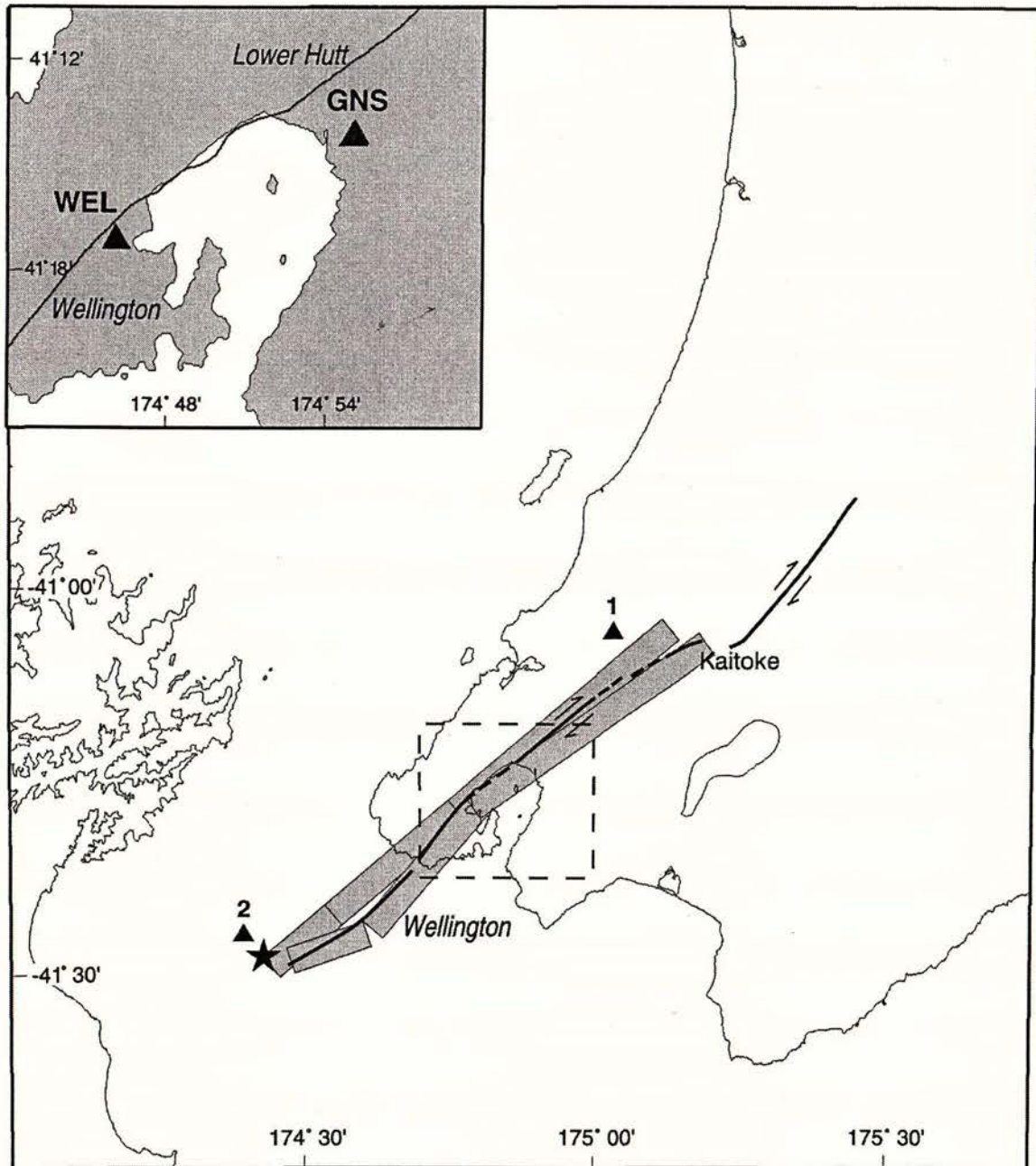


Figure 1 Map view of the southern North Island including the Wellington region. The solid black line shows the Wellington fault, while the shaded rectangles are the map projections of the modelled fault dislocations. Solid triangles mark the receiver sites used in the complex rupture simulations. The star represents the reference origin, used as the rupture initiation point for smooth ruptures. The insert is a magnified view of Wellington and Lower Hutt, showing the two station locations (triangles) used as receiver sites for the smooth rupture synthetics.

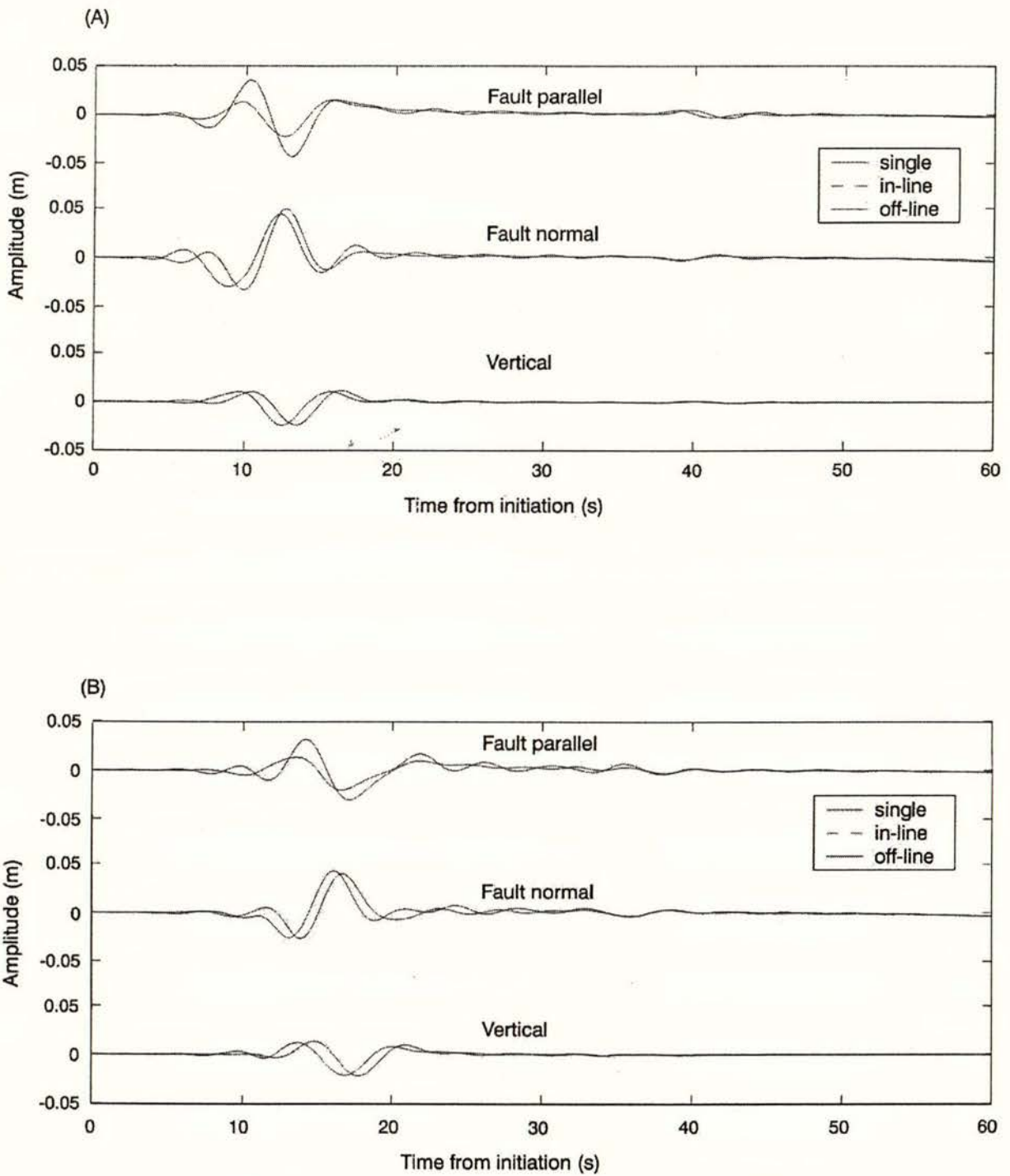


Figure 2 Displacement waveforms for a single rupture model (red line), the three colinear segmented fault model (dashed green line), and the three variable strike segmented fault model for stations at a) WEL and b) GNS.

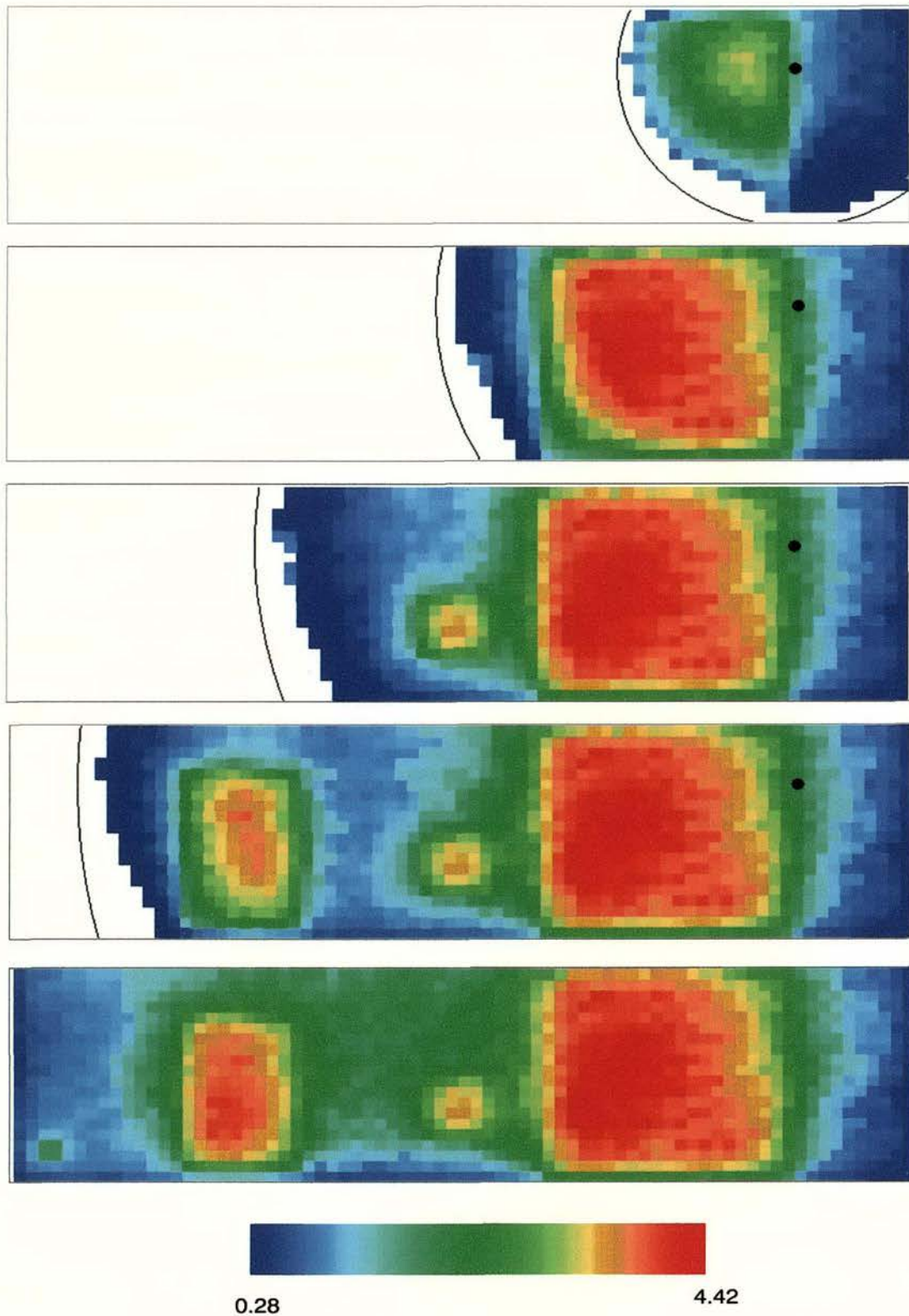


Figure 3 Distribution of slip for Event 1, generated by synthetic seismicity techniques, over the model fault plane at 4 s intervals (except the last, which is the final slip distribution). The slip magnitude is shown, but in the case of this fault horizontal slip predominates. The black spot indicates the rupture initiation point.

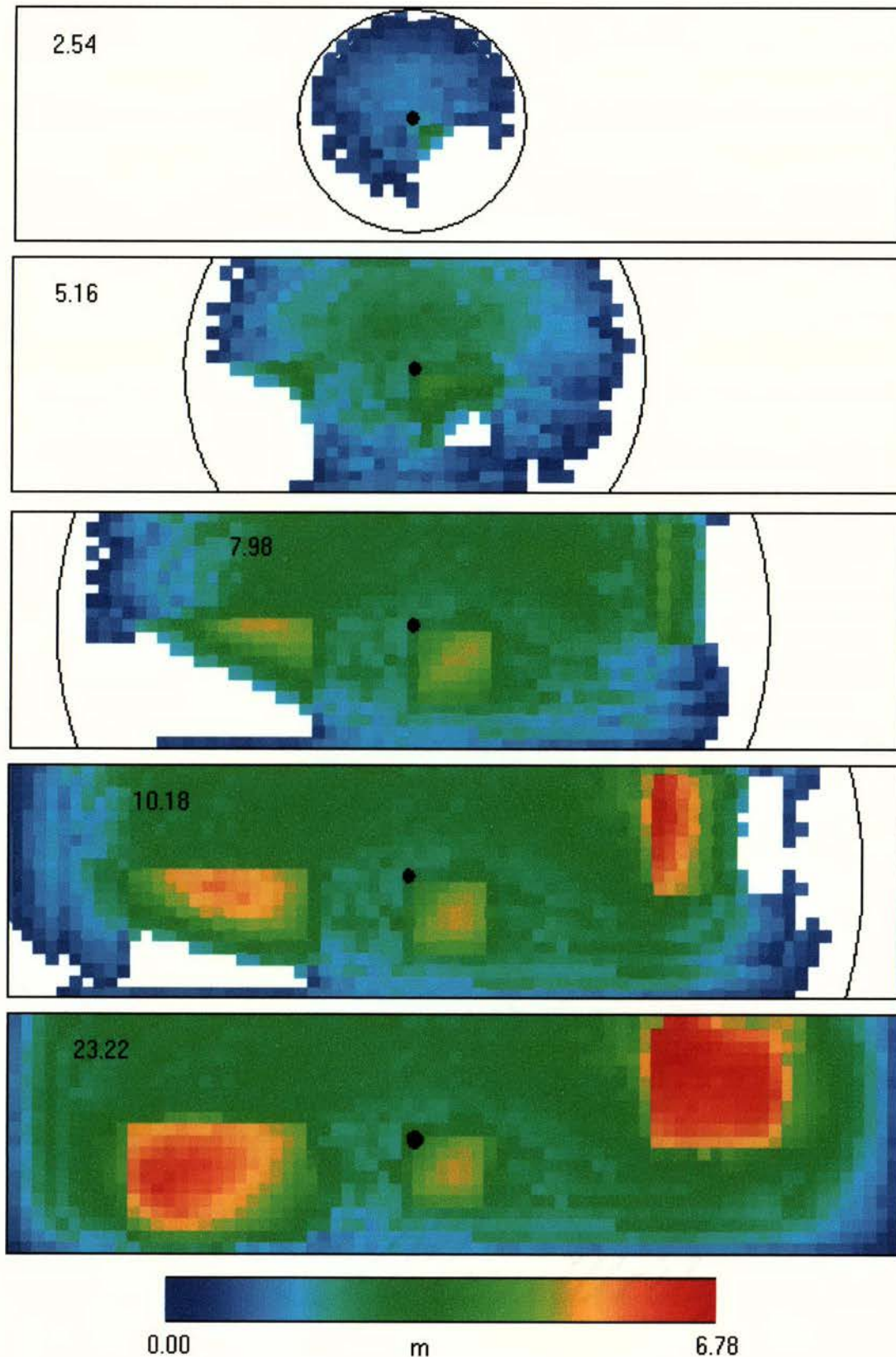


Figure 4 Distribution of slip for Event 2, generated by synthetic seismicity techniques, over the model fault plane at the intervals shown by the annotated numbers, in seconds. The last frame shows the final slip distribution. The slip magnitude is shown, but in the case of this fault horizontal slip predominates. The black spot indicates the rupture initiation point.

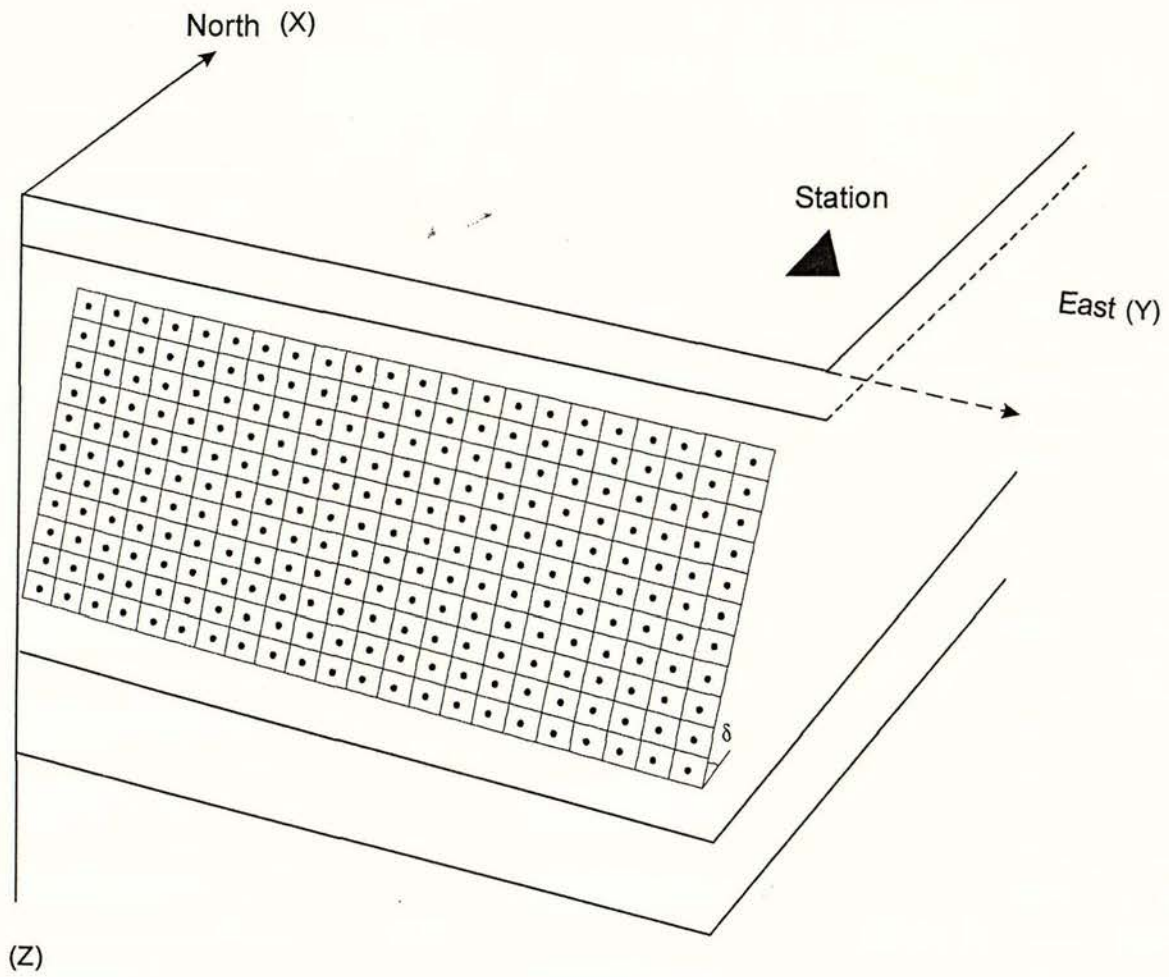


Figure 5 Schematic diagram of the model geometry showing a fault with dip, δ , divided into subfaults. The north and east axes correspond to the x and y directions in our equations, respectively, not to true geographic north and east.

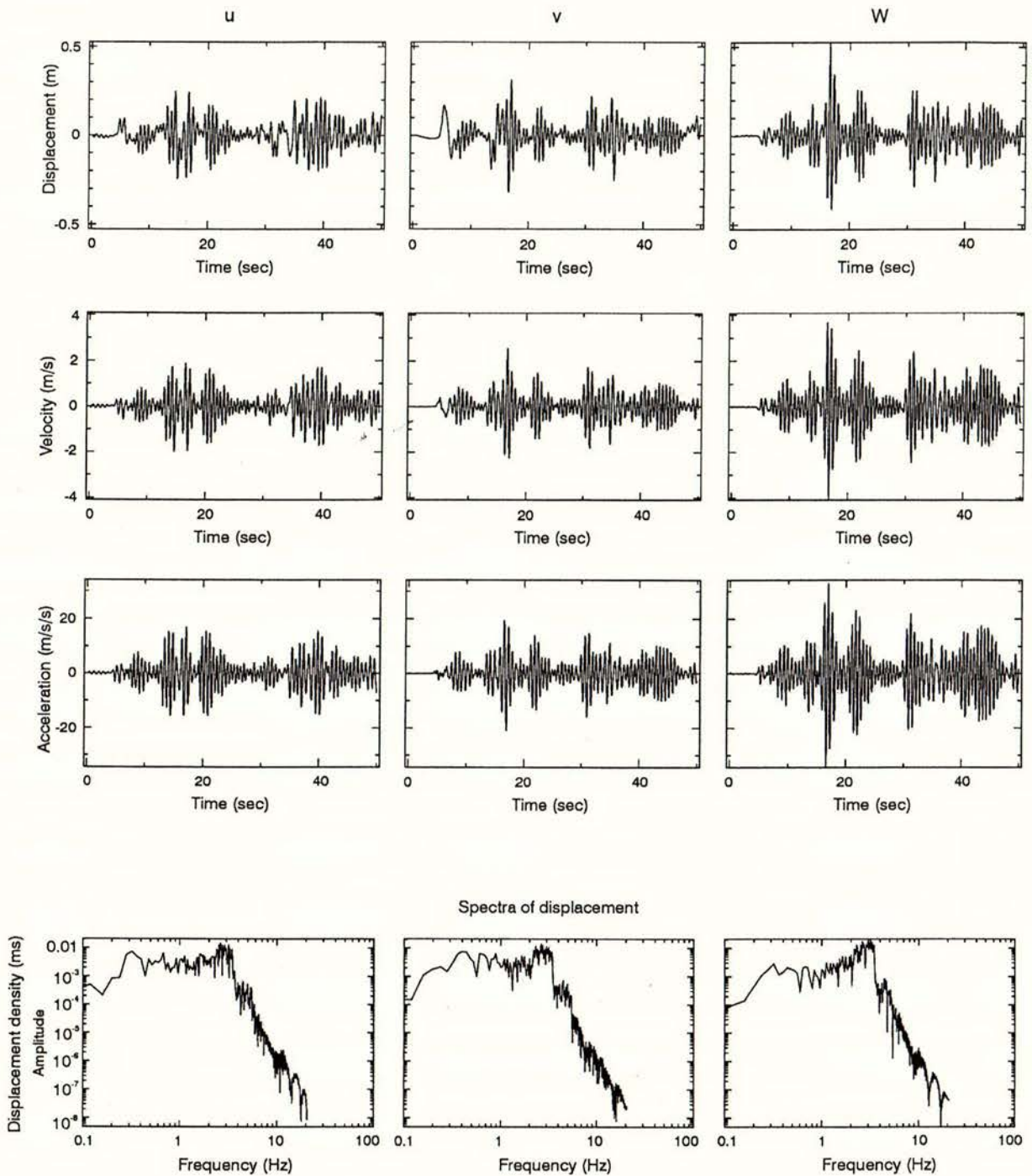


Figure 6 Displacement, velocity, and acceleration seismograms and displacement spectra for fault-normal (u), fault-parallel (v), and vertical (w) components of ground motion for a Wellington fault rupture synthesised from the slip time history for Event 1 using a finite fault calculation on each of 1,500 subfaults. The receiver is located near the rupture initiation at the NE end of the fault (Fig. 1, Site 1).

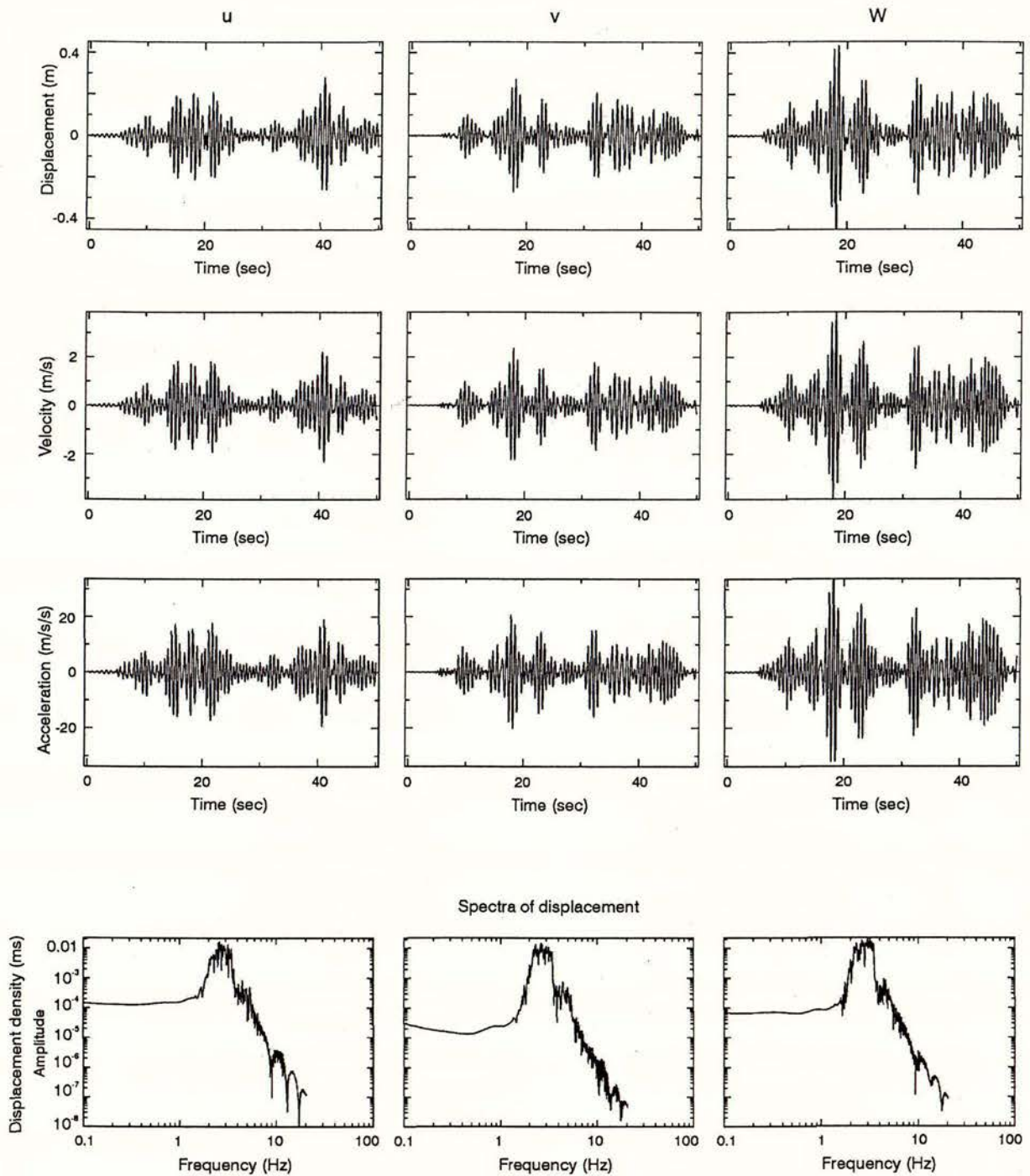


Figure 7 Displacement, velocity, and acceleration seismograms and displacement spectra for fault-normal (u), fault-parallel (v), and vertical (w) components of ground motion for a Wellington fault rupture synthesised from the slip time history for Event 1 using a finite fault calculation on each of 1,500 subfaults. The data have been high pass filtered with a filter corner frequency at 1 Hz. The receiver is located near the rupture initiation at the NE end of the fault (Fig. 1, Site 1).

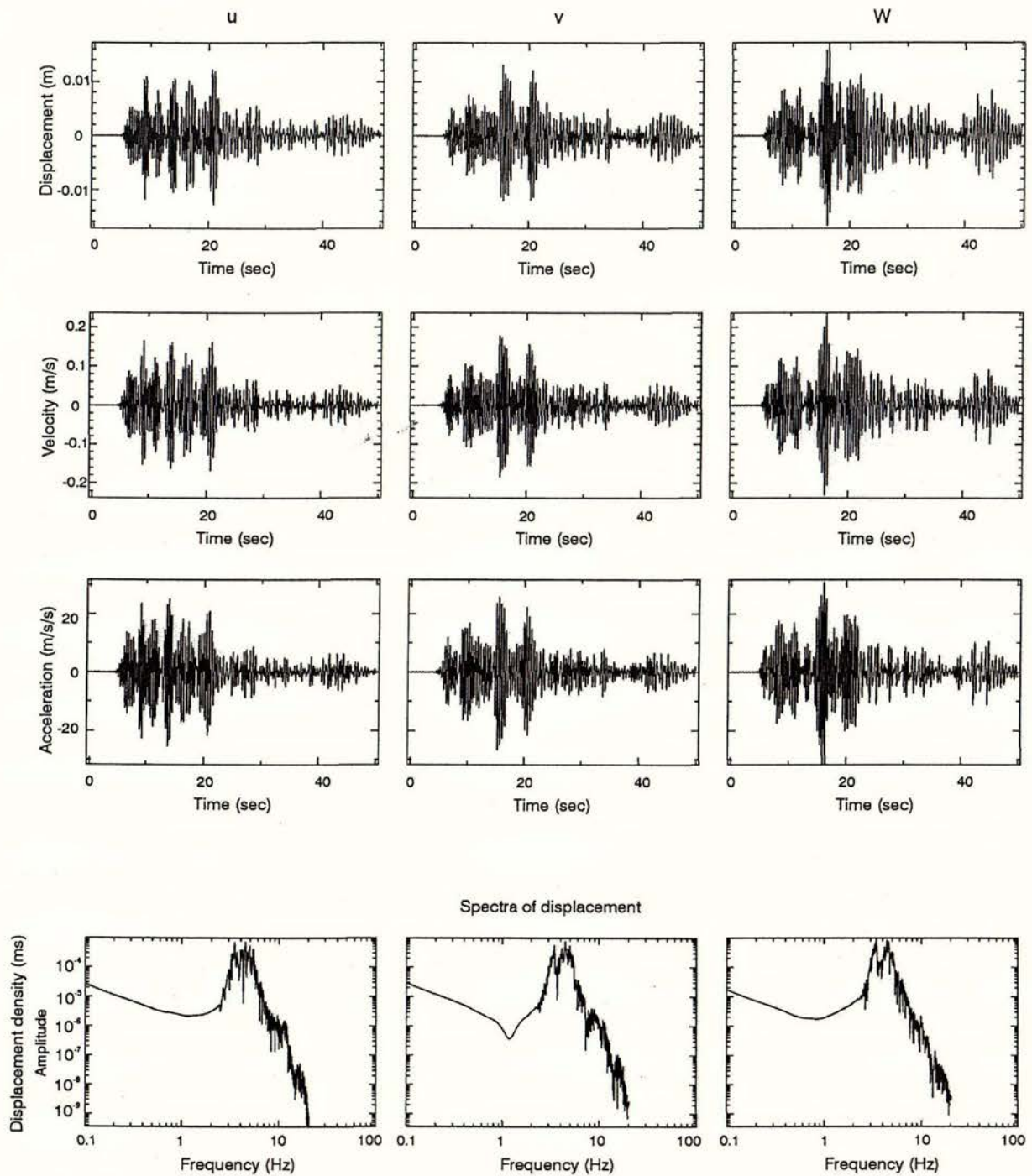


Figure 8 Displacement, velocity, and acceleration seismograms and displacement spectra for fault-normal (u), fault-parallel (v), and vertical (w) components of ground motion for a Wellington fault rupture synthesised from the slip time history for Event 1 using a finite fault calculation on each of 1,500 subfaults. The data have been high pass filtered with a filter corner frequency at 2 Hz. The receiver is located near the rupture initiation at the NE end of the fault (Fig. 1, Site 1).

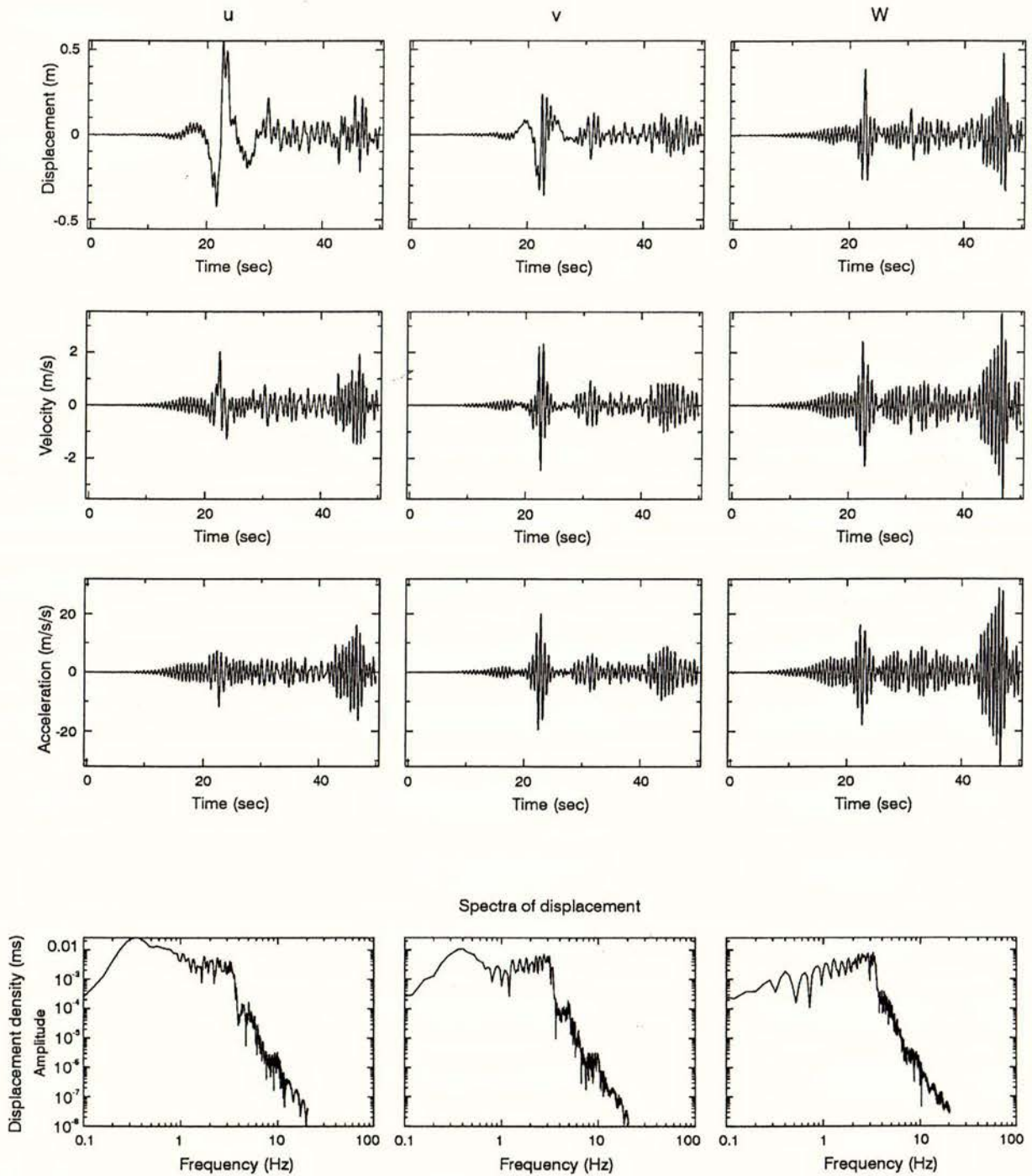


Figure 9 Displacement, velocity, and acceleration seismograms and displacement spectra for fault-normal (u), fault-parallel (v), and vertical (w) components of ground motion for a Wellington fault rupture synthesised from the slip time history for Event 1 using a finite fault calculation on each of 1,500 subfaults. The receiver is located near the rupture termination at the SW end of the fault (Fig. 1, Site 2).

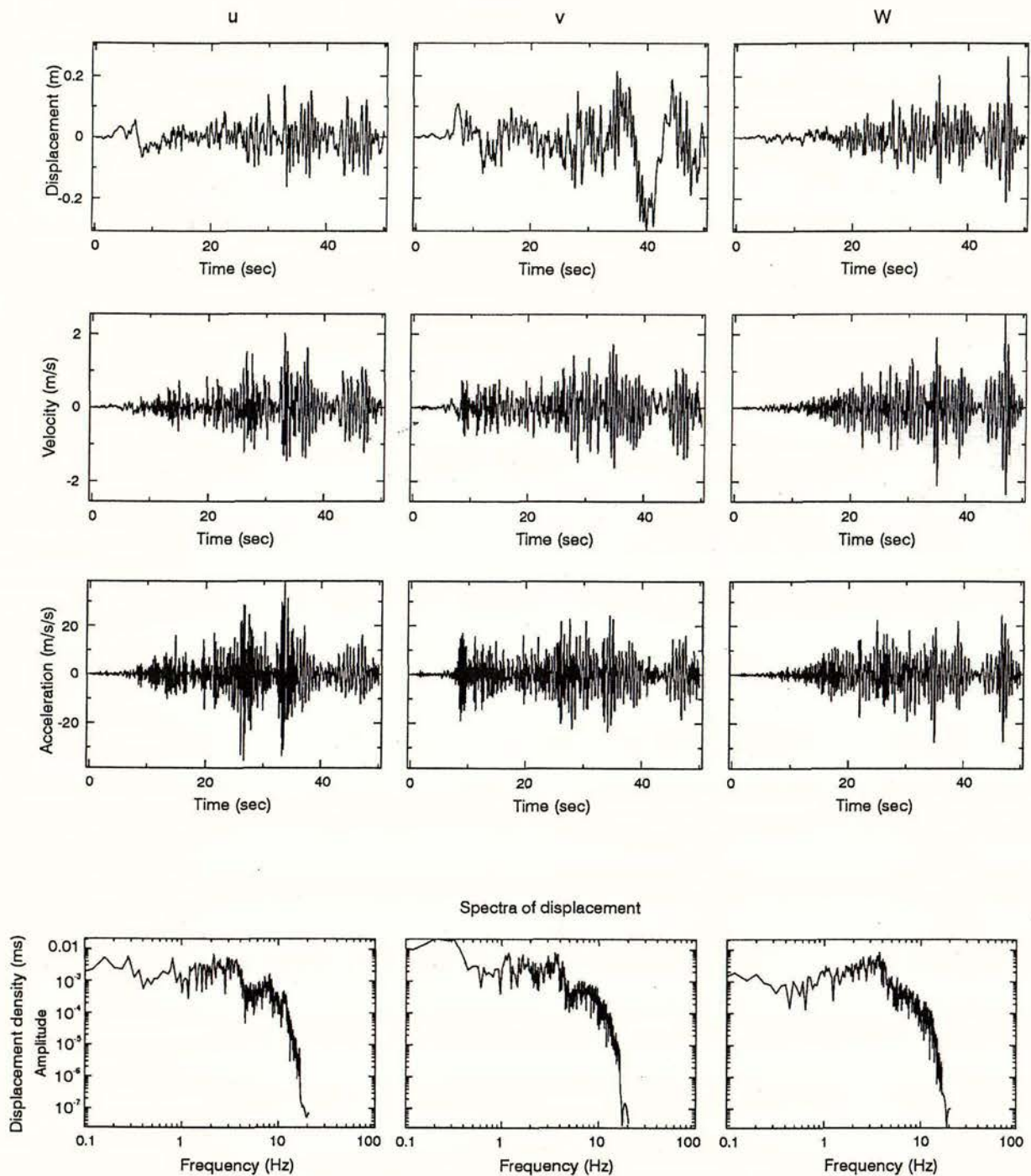


Figure 10 Displacement, velocity, and acceleration seismograms and displacement spectra for fault-normal (u), fault-parallel (v), and vertical (w) components of ground motion for a Wellington fault rupture synthesised from the slip time history for Event 1 using a point source with directivity correction on each of 1,500 subfaults. The receiver is located near the rupture initiation at the NE end of the fault (Fig. 1, Site 1).

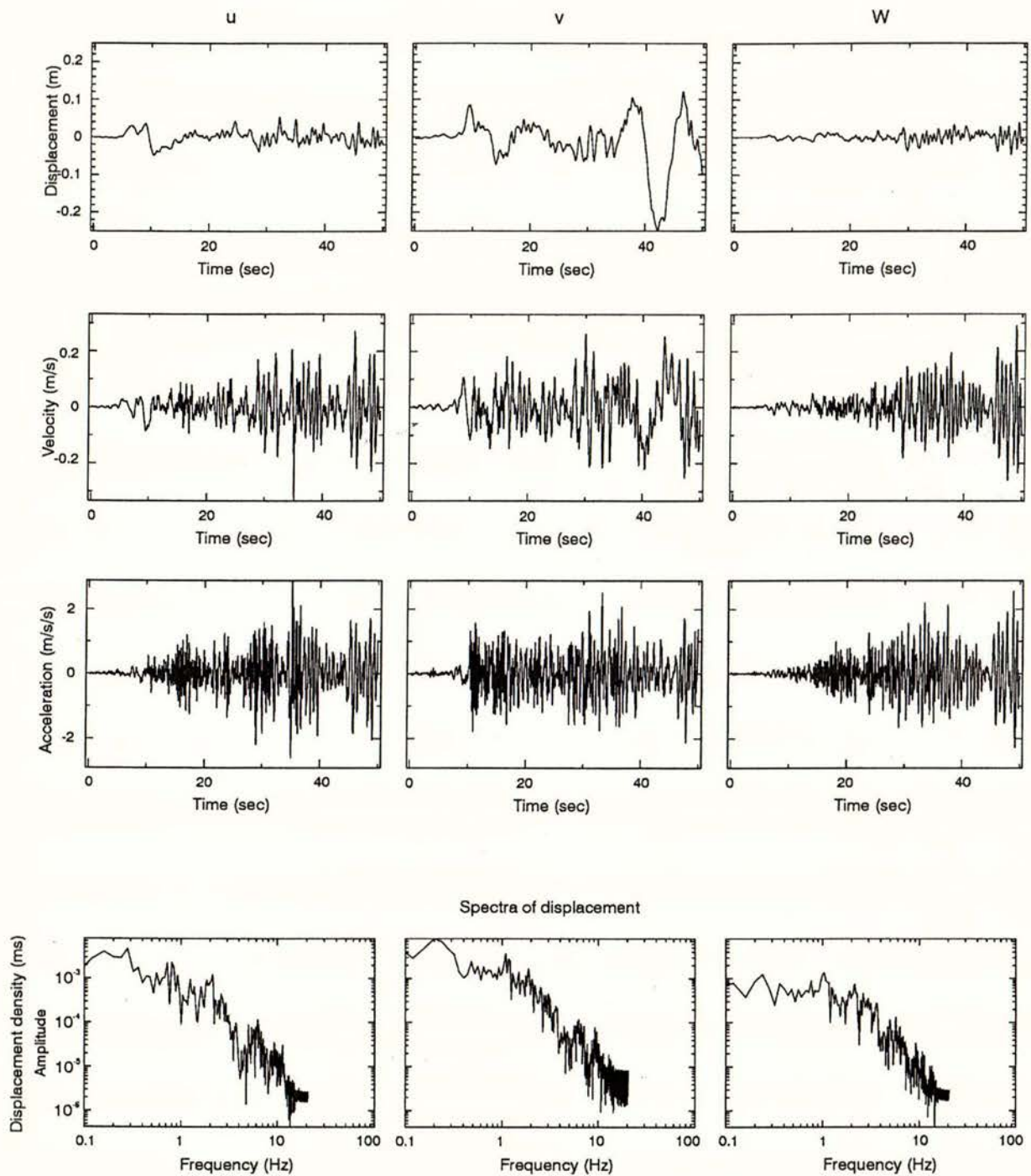


Figure 11 Displacement, velocity, and acceleration seismograms and displacement spectra for fault-normal (u), fault-parallel (v), and vertical (w) components of ground motion for a Wellington fault rupture synthesised from the slip time history for Event 1 using a point source with directivity correction on each of 1,500 subfaults. The receiver is located near the rupture initiation at the NE end of the fault (Fig. 1, Site 1). This figure differs from Figure 10 in that here a rise time of 0.5 s has been used compared to 0.1 s in Figure 10 and subsequent figures.

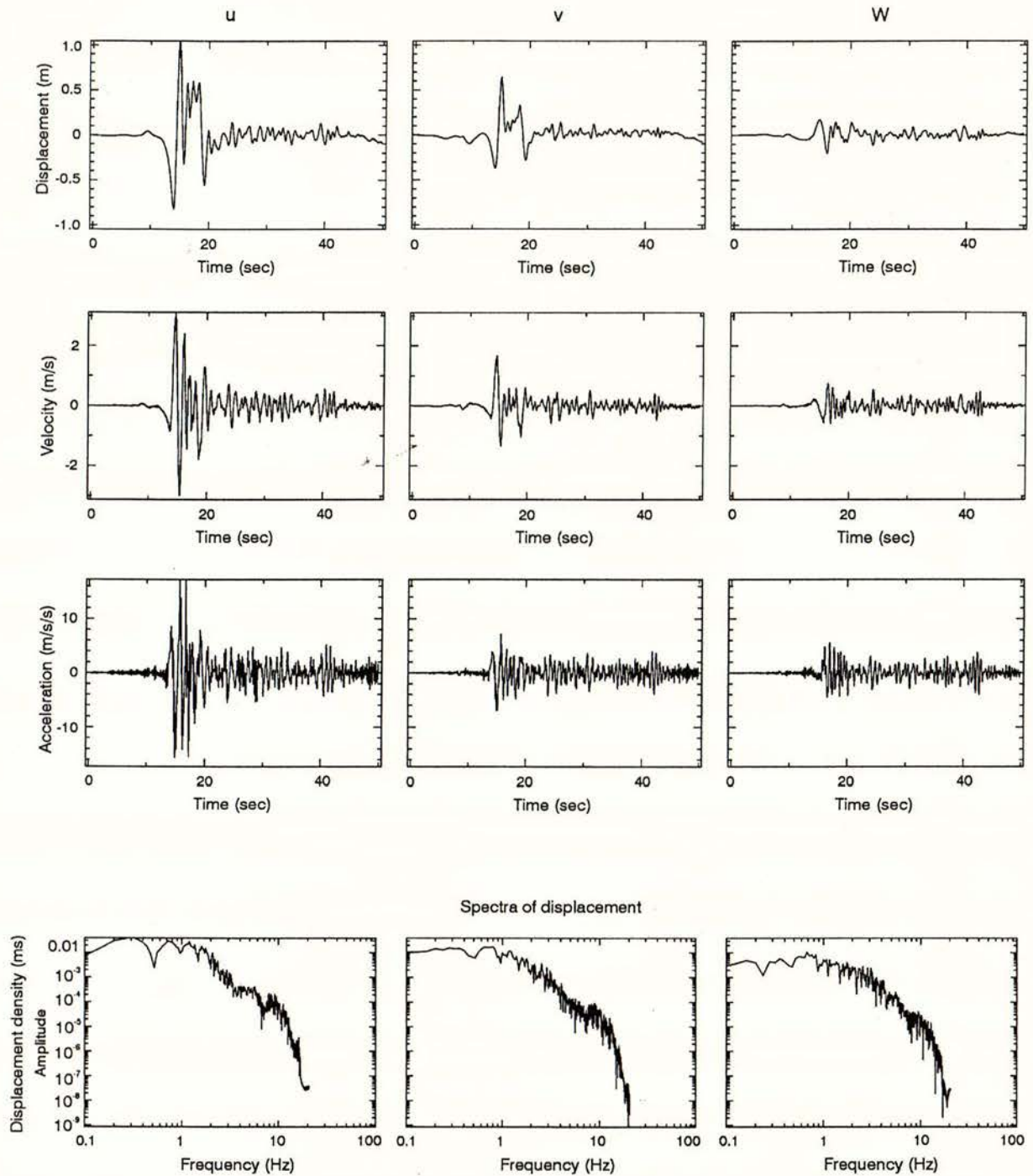


Figure 12 Displacement, velocity, and acceleration seismograms and displacement spectra for fault-normal (u), fault-parallel (v), and vertical (w) components of ground motion for a Wellington fault rupture synthesised from the slip time history for Event 1 using a point source with directivity correction on each of 1,500 subfaults. The receiver is located near the rupture termination at the SW end of the fault (Fig. 1, Site 2).

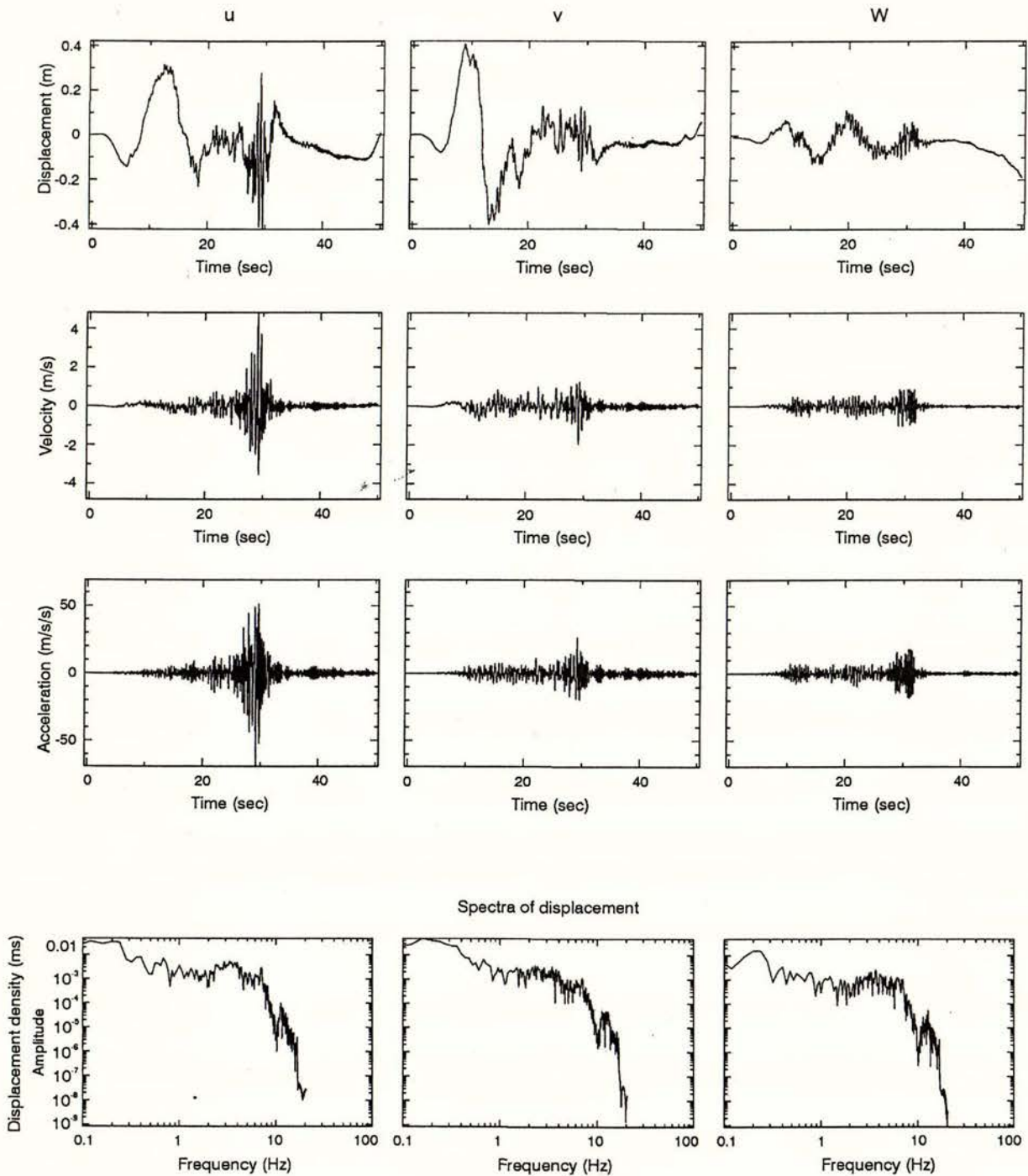


Figure 13 Displacement, velocity, and acceleration seismograms and displacement spectra for fault-normal (u), fault-parallel (v), and vertical (w) components of ground motion for a Wellington fault rupture synthesised from the slip time history for Event 2 using a point source with directivity correction on each of 1,500 subfaults. The receiver is located near the rupture initiation at the NE end of the fault (Fig. 1, Site 1).

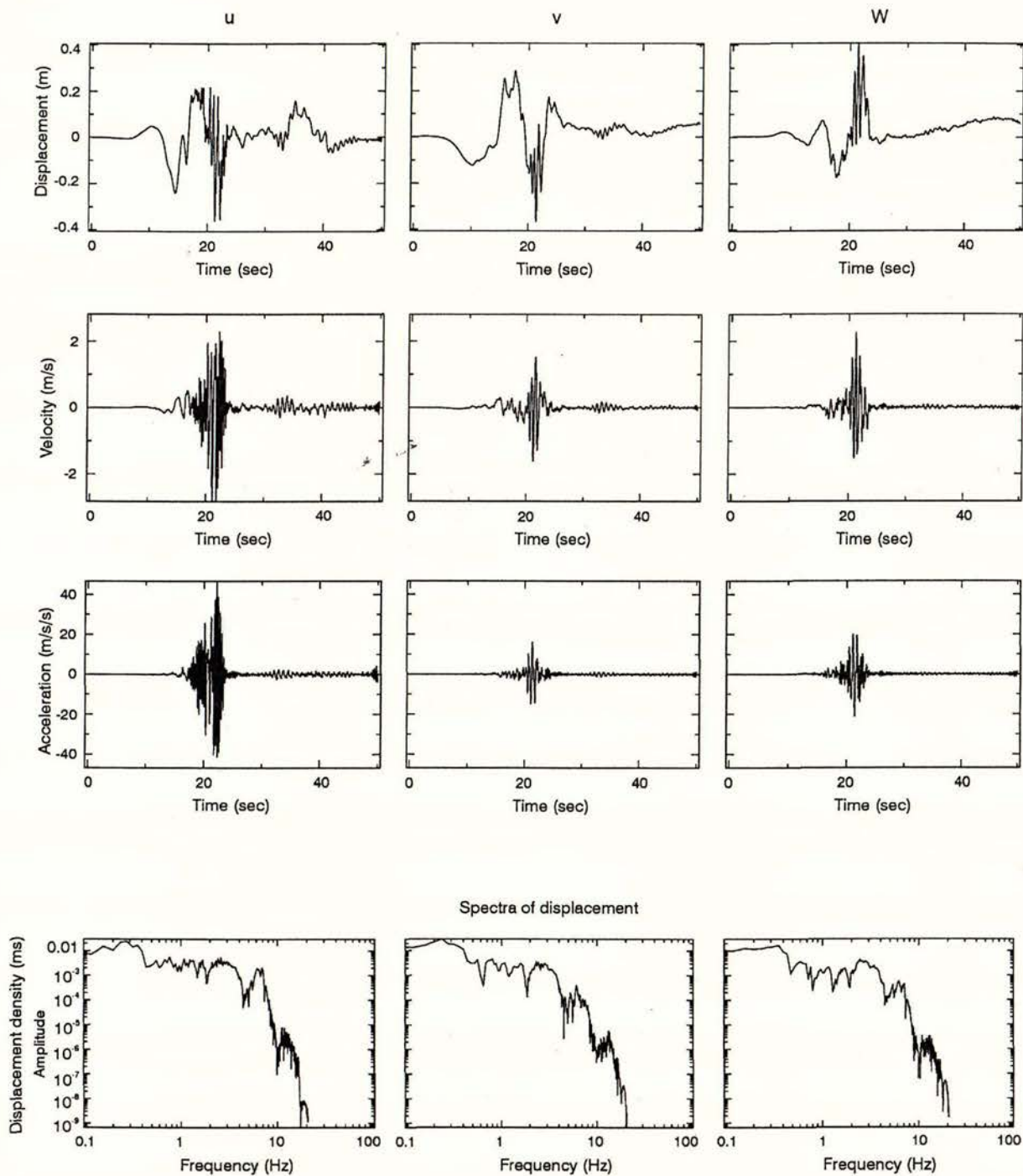


Figure 14 Displacement, velocity, and acceleration seismograms and displacement spectra for fault-normal (u), fault-parallel (v), and vertical (w) components of ground motion for a Wellington fault rupture synthesised from the slip time history for Event 2 using a point source with directivity correction on each of 1,500 subfaults. The receiver is located near the rupture termination at the SW end of the fault (Fig. 1, Site 2).



8.0 APPENDIX

A.1 Rectangular subfault

Referring to Figure 1 and equations (2), the analytical expressions of R_P^\pm , R_{SV}^\pm , and R_{SH}^\pm are (Bouchon, 1979; Chin, 1992):

$$R_P^\pm = \frac{iD}{2L_x L_y k_\beta^2} M_P^\pm \mathfrak{R}_P^\mp(L) \mathfrak{R}_P^\mp(W) E(k_x, k_y) \times \exp[\pm i\nu(z - z_r)] \quad (A1)$$

$$R_{SV}^\pm = \frac{iD}{2L_x L_y k_\beta^2} M_{SV}^\pm \mathfrak{R}_S^\mp(L) \mathfrak{R}_S^\mp(W) E(k_x, k_y) \times \exp[\pm i\gamma(z - z_r)]$$

$$R_{SH}^\pm = \frac{iD}{2L_x L_y k_\beta^2} M_{SH}^\pm \mathfrak{R}_S^\mp(L) \mathfrak{R}_S^\mp(W) E(k_x, k_y) \times \exp[\pm i\gamma(z - z_r)]$$

where:

$$\mathfrak{R}_P^\mp(L) = \frac{\exp iL(a_1 k_x + b_1 k_y \mp c_1 \nu - \omega/v_r) - 1}{a_1 k_x + b_1 k_y \mp c_1 \nu - \omega/v_r}$$

$$\mathfrak{R}_P^\mp(W) = \frac{\exp iW(a_2 k_x + b_2 k_y \mp c_2 \nu) - 1}{a_2 k_x + b_2 k_y \mp c_2 \nu}$$

$$\mathfrak{R}_S^\mp(L) = \frac{\exp iL(a_1 k_x + b_1 k_y \mp c_1 \gamma - \omega/v_r) - 1}{a_1 k_x + b_1 k_y \mp c_1 \gamma - \omega/v_r}$$

$$\mathfrak{R}_S^\mp(W) = \frac{\exp iW(a_2 k_x + b_2 k_y \mp c_2 \gamma) - 1}{a_2 k_x + b_2 k_y \mp c_2 \gamma}$$

$$E(k_x, k_y) = \exp[-ik_x(x - x_r) - ik_y(y - y_r)]$$



$$M_P^\pm = M_{xx}k_x^2 + 2M_{xy}k_xk_y/\nu \mp 2M_{xz}k_x + M_{yy}k_y^2/\nu \pm 2M_{yz}k_y + M_{zz}\nu$$

$$M_{SV}^\pm = \pm M_{xx}k_x^2/k \pm 2M_{xy}k_xk_y/k + M_{xz}k_x(2k^2 - k_\beta^2)/\gamma k \pm M_{yy}k_y^2/k + \\ M_{yz}k_y(2k^2 - k_\beta^2)/\gamma k \mp M_{zz}k$$

$$M_{SH}^\pm = M_{xx}k_xk_y/\gamma + M_x(k_x^2 + k_y^2)/\gamma \mp M_{xz}k_y - M_{yy}k_xk_y/\gamma \pm M_{yz}k_x$$

and

$$a_1 = \cos \lambda \cos \phi + \sin \lambda \cos \delta \sin \phi$$

$$a_2 = -\sin \lambda \cos \phi + \cos \lambda \cos \delta \sin \phi$$

$$b_1 = \cos \lambda \sin \phi - \sin \lambda \cos \delta \cos \phi$$

$$b_2 = -\sin \lambda \sin \phi - \cos \lambda \cos \delta \cos \phi$$

$$c_1 = -\sin \lambda \sin \delta$$

$$c_2 = -\cos \lambda \sin \delta$$

with $\nu = (k_\alpha^2 - k^2)^{1/2}$, $\gamma = (k_\beta^2 - k^2)^{1/2}$, $k_\alpha = \omega/\alpha$, $k_\beta = \omega/\beta$, and $k = (k_x^2 + k_y^2)^{1/2}$, in which α and β are the velocities of the P and S waves, respectively, and k is wavenumber.

The quantities M_{ij} ($i,j=x,y,z$) are the components of the moment tensor, defined as (Aki & Richards, 1980):

$$M_{xx} = -M_0[\cos \lambda \sin \delta \sin 2\phi + \sin \lambda \sin 2\delta \sin^2 \phi]$$

$$M_{xy} = M_0[\cos \lambda \sin \delta \cos 2\phi + 0.5 \sin \lambda \sin 2\delta \sin 2\phi]$$

$$M_{xz} = -M_0[\cos \lambda \cos \delta \cos \phi + \sin \lambda \cos 2\delta \sin \phi]$$

$$M_{yy} = M_0[\cos \lambda \sin \delta \sin^2 \phi - \sin \lambda \sin 2\delta \cos^2 \phi]$$

$$M_{yx} = -M_0[\cos \lambda \cos \delta \sin \phi - \sin \lambda \cos 2\delta \cos \phi]$$

$$M_{zz} = M_0[\sin \lambda \sin 2\delta]$$



A.2 Double-couple point source

Referring to equations (5), the radiation factors for a double-couple point source are :

$$R_p^\pm = \frac{iDk}{4\pi\nu L_\pi k_\beta^2} \{A_1 J_0(kr) + A_2 J_1(kr)\} \quad (A2)$$

$$R_{SV}^\pm = \frac{iD}{4\pi L_\pi k_\beta^2} \{B_1 J_0(kr) + B_2 J_1(kr)\}$$

$$R_{SH}^\pm = \frac{iD}{4\pi L_\pi \gamma} \{C_1 J_0(kr) + C_2 J_1(kr)\}$$

with

$$A_1 = k^2(\sin^2 \phi M_{xx} + \sin 2\phi M_{xy} + \cos^2 \phi M_{yy}) + \nu^2 M_{zz}]$$

$$A_2 = k(\cos 2\phi M_{xx} - 2 \sin 2\phi M_{xy} - \cos 2\phi M_{yy})/r \pm 2i\nu k(\sin \phi M_{xz} + \cos \phi M_{yz})]$$

$$B_1 = \pm k^2(\sin^2 \phi M_{xx} + \sin 2\phi M_{xy} + \cos^2 \phi M_{yy} - M_{zz})$$

$$B_2 = \pm k(\cos 2\phi M_{xx} - 2 \sin 2\phi M_{xy} - \cos 2\phi M_{yy})/r - ik(2k^2 - k_\beta^2)(\sin \phi M_{xz} + \cos \phi M_{yz})/\gamma$$

$$C_1 = k(M_{xx} + \cos 2\phi M_{xy} - M_{yy})/2$$

$$C_2 = (M_{xx} - 2 \cos 2\phi M_{xy} + M_{yy})/r \pm i\gamma(\cos \phi M_{xz} - \sin \phi M_{yz})$$

Institute of Geological & Nuclear Sciences Limited

Gracefield Research Centre
69 Gracefield Road
PO Box 30 368
Lower Hutt
New Zealand
Phone +64-4-570 1444
Fax +64-4-570 4600

Rafter Research Centre
30 Gracefield Road
PO Box 31 312
Lower Hutt
New Zealand
Phone +64-4-570 4637
Fax +64-4-570 4657

Dunedin Research Centre
764 Cumberland Street
Private Bag 1930
Dunedin
New Zealand
Phone +64-3-477 4050
Fax +64-3-477 5232

Wairakei Research Centre
State Highway 1, Wairakei
Private Bag 2000
Taupo
New Zealand
Phone +64-7-374 8211
Fax +64-7-374 8199

For more information visit the GNS website
<http://www.gns.cri.nz>

A Crown Research Institute

Cover photographs from GNS photo library